

Simulation-Based Inference Benchmark for LSST Weak Lensing Cosmology

Justine Zeghal¹, Denise Lanzieri^{2,6}, François Lanusse^{3,7}, Alexandre Boucaud¹, Gilles Louppe⁴, Eric Aubourg⁵,
Adrian E. Bayer^{8,7}, and The LSST Dark Energy Science Collaboration

¹ Université Paris Cité, CNRS, Astroparticule et Cosmologie, F-75013 Paris, France

² Université Paris Cité, Université Paris-Saclay, CEA, CNRS, AIM, F-91191, Gif-sur-Yvette, France

³ Université Paris-Saclay, Université Paris Cité, CEA, CNRS, AIM, 91191, Gif-sur-Yvette, France

⁴ University of Liège, Liège, Belgium

⁵ Université Paris Cité, CNRS, CEA, Astroparticule et Cosmologie, F-75013 Paris, France

⁶ Sony Computer Science Laboratories - Rome, Joint Initiative CREF-SONY, Centro Ricerche Enrico Fermi, Via Panisperna 89/A, 00184, Rome, Italy

⁷ Center for Computational Astrophysics, Flatiron Institute, 162 5th Ave, New York, NY, 10010, USA

⁸ Department of Astrophysical Sciences, Princeton University, Peyton Hall, 4 Ivy Lane, Princeton, NJ 08544, USA

Received XXXX; accepted XXXX

ABSTRACT

Context. Standard cosmological analysis, which relies on two-point statistics, fails to extract the entire information embedded in cosmological data. This limits our ability to constrain with precision cosmological parameters. With the willingness to use modern analysis techniques to match the power of upcoming telescopes, recent years have seen a paradigm shift from *analytical likelihood-based* to *simulation-based inference*. However, such methods require a large number of costly simulations.

Aims. We focus on full-field inference, which is considered the optimal form of inference as it enables recovery of cosmological constraints from simulations without any loss of cosmological information. Our objective is to review and benchmark several ways of conducting full-field inference to gain insight into the number of simulations required for each method. Specifically, we make a distinction between *explicit inference* methods that require an explicit form of the likelihood such that it can be evaluated and thus sampled through sampling schemes and *implicit inference* methods that can be used when only an implicit version of the likelihood is available through simulations. Moreover, it is crucial for explicit full-field inference to use a differentiable forward model. Similarly, we aim to discuss the advantages of having differentiable forward models for implicit full-field inference.

Methods. We use the `sbi_lens` package which provides a fast and differentiable log-normal forward model that can generate convergence maps at the quality expected for the tenth year of LSST. This fast forward model enables us to compare explicit and implicit full-field inference with and without gradient. The former is achieved by sampling the forward model through the No U-Turns (NUTS) sampler. The latter starts by compressing the data into sufficient statistics and uses the Neural Likelihood Estimation (NLE) algorithm and the one augmented with gradient (∂ NLE) to learn the likelihood distribution and then sample the posterior distribution.

Results. We perform a full-field analysis on LSST Y10 like weak lensing simulated log-normal convergence maps where we constrain $(\Omega_c, \Omega_b, \sigma_8, h_0, n_s, w_0)$. We demonstrate that explicit full-field and implicit full-field inference yield consistent constraints. Explicit full-field inference requires 630 000 simulations with our particular sampler which corresponds to 400 independent samples. Implicit full-field inference requires a maximum of 101 000 simulations split into 100 000 simulations to build neural-based sufficient statistics (this number of simulations is not fine tuned) and 1 000 simulations to perform inference using implicit inference. Additionally, while differentiability is very useful for explicit full-field inference we show that, for this specific case, our way of exploiting the gradients does not significantly help implicit full-field inference.

Key words. methods: statistical - gravitational lensing: weak – cosmology: large-scale structure of Universe

1. Introduction

Understanding the cause of the observed accelerated expansion of the Universe is currently a major topic in cosmology. The source of this acceleration has been dubbed Dark Energy, but its nature is still unknown. Dark Energy cannot be directly observed but several observational probes can be used to understand better its characteristics, with weak gravitational lensing, in which background galaxies are sheared by foreground matter, being one of the most powerful. This phenomenon is sensitive to both the geometry of the Universe and the growth of structure, which both depend on the cosmological parameters of the dark energy model. Many photometric galaxy surveys such

as CFHTLenS (Erben et al. 2013), KiDS (de Jong et al. 2012), DES (Flaugher 2005), and HSC (Aihara et al. 2017), have already demonstrated its constraining power on the matter density Ω_m and fluctuation amplitude σ_8 parameters. Upcoming weak lensing surveys (LSST (Ivezić et al. 2019), Roman (Spergel et al. 2015), Euclid (Laureijs et al. 2011)) are expected to be larger and deeper allowing us to refine our estimations even further.

In cosmological inference, a significant challenge lies in the absence of an analytic likelihood $p(x|\theta)$ to recover cosmological parameters θ from the data x . Most of the mathematical inference frameworks proposed to overcome this problem are based on two-stage inference: compression of the data into summary statistics $t = f(x)$ and then Bayesian inference to obtain the

posterior $p(\theta|t)$. The most famous one is the two-point statistics analysis (e.g., Kilbinger 2015). It uses as a summary statistic t the two-point correlation function or its analog in Fourier space, the power spectrum. Then, the inference part of the analysis is performed using the corresponding analytic Gaussian likelihood $p(t|\theta)$ which is sampled through Markov Chain Monte Carlo (MCMC). On large scales, the Universe remains close to a Gaussian field and the 2-point function is a near sufficient statistic to extract cosmological information. However, on small scales where non-linear evolution gives rise to a highly non-Gaussian field, this summary statistic is not sufficient anymore.

At a time when future surveys will access small scales, we need to investigate summary statistics that can capture non-Gaussianities. This has led to a new class of statistics, known as higher-order statistics, including, for example, lensing peak counts (e.g., Liu et al. 2015a,b; Lin & Kilbinger 2015; Kacprzak et al. 2016; Peel et al. 2017; Shan et al. 2018; Martinet et al. 2018; Ajani et al. 2020; Harnois-Déraps et al. 2021; Zürcher et al. 2022), 3-point statistics (e.g., Takada & Jain 2004; Semboloni et al. 2011; Fu et al. 2014; Rizzato et al. 2019; Halder et al. 2021) and machine learning compression (e.g., Charnock et al. 2018; Fluri et al. 2018; Gupta et al. 2018; Ribli et al. 2019; Jeffrey et al. 2021; Fluri et al. 2022; Akhmetzhanova et al. 2024; Jeffrey et al. 2024), all with varying degrees of signal extraction power. Most of the time, no analytical models $p(t|x)$ exist and these statistics are usually assumed to be Gaussian distributed leading to potentially biased inference or inaccurate uncertainty estimation. On top of that, since no analytical function $t = g(\theta)$ to map cosmological parameters to the summary statistic exists, the inference part requires a large number of very costly simulations $x \sim p(x|\theta)$ (with $p(x|\theta)$ a simulator) to compute the summary statistics $t = f(x)$. This is in addition to the number of simulations already required to compute the covariance matrix.

Full-field inference (e.g., Schneider et al. 2015; Alsing et al. 2016, 2017; Böhm et al. 2017; Porqueres et al. 2021, 2022, 2023; Junzhe Zhou et al. 2023; Dai & Seljak 2024; Lanzieri et al. 2024), aims to perform inference from simulations without any loss of information. This means no loss of information coming from a compression step and no loss of information coming from assumptions on the likelihood function employed for inference. Hence the quality of the learned posterior is solely tied to the forward model’s accuracy. This paper focuses on this particular kind of inference.

Depending on the nature of the forward model $p(x|\theta)$, one can either perform explicit inference or implicit inference. The former refers to inference methods that can be used when the likelihood function $p(x = x_0|\theta)$ can be evaluated for different θ and sampling schemes can thus be employed. The latter can be used when only an implicit version of the likelihood is available through a set of simulations (θ, x) . Implicit inference, also known as likelihood-free inference or simulation-based inference, commonly recasts the inference problem as a neural density optimization problem where the distribution is learned and can be evaluated for all θ and x . There exist different flavors of implicit inference, one aims to learn the likelihood function $p(x|\theta)$ (e.g., Wood 2010; Papamakarios et al. 2018b; Lueckmann et al. 2018; Sharrock et al. 2022) or the likelihood ratio $r(\theta, x) = p(x|\theta)/p(x)$ (e.g., Izbicki et al. 2014; Cranmer et al. 2015; Thomas et al. 2016; Hermans et al. 2020; Durkan et al. 2020; Miller et al. 2023). This learned likelihood or likelihood ratio can now be evaluated and sampling methods can be used to get the posterior $p(\theta|x)$. Others choose to directly approximate the posterior distribution $p(\theta|x)$ (e.g., Blum & François 2009; Papamakarios

& Murray 2018; Lueckmann et al. 2017; Greenberg et al. 2019; Wildberger et al. 2023).

Explicit inference applied in the context of full-field inference is known as Bayesian Hierarchical/Forward Modeling. Because of the high complexity and dimension of the field-based likelihood, sampling schemes guided by the gradient information $\nabla_{\theta} \log p(x|\theta)$ are typically used to explore the parameter space in a more efficient way. This motivates the development of differentiable forward models $p(x|\theta)$. Naturally, we could ask, could these gradients also help implicit inference methods for full-field inference? Specifically, Brehmer et al. (2020) and Zeghal et al. (2022) proposed implicit inference methods to leverage the gradient information from the forward model while approximating the likelihood, the likelihood ratio, or the posterior distribution. They showed that this additional information helps to constrain the target distribution and thus improve sample efficiency.

In summary, within the context of LSST Y10, this paper aims to answer the following questions:

- Is the differentiability of the forward model a useful asset for full-field implicit inference?
- Which methods allow full-field inference with the fewest simulations?

To meet the full-field criterion, we focus our benchmark analysis on two inference strategies:

- Explicit full-field inference: we sample our forward model through the use of the Hamiltonian Monte Carlo (HMC) sampling method. Specifically, we use the No-U-Turn (NUTS) algorithm.
- Implicit full-field inference: after compressing the simulations into sufficient statistics, we compare the Neural Likelihood Estimation (NLE) and Neural Likelihood Estimation augmented with gradients (∂ NLE).

For the implicit inference strategy, maps are compressed using an optimal neural compression approach: we train a Convolutional Neural Network (CNN) by maximizing the mutual information between the cosmological parameters and the summary statistic (e.g. Jeffrey et al. 2021; see Lanzieri et al. 2024 for a review on optimal neural compression strategies). In this study, we separate the compression process from the inference process and concentrate solely on the amount of simulations necessary for inference. We will explain why in subsection 6.3.

We use the same forward model to benchmark the different inference strategies and use the same fiducial data x_0 . Our forward model is a differentiable field-based likelihood that can be evaluated and can generate simulations such that both approaches explicit and implicit can be performed. Specifically, it is a log-normal model that produces LSST Y10-like weak lensing convergence maps. The cosmological parameters θ that we aim to constrain are $(\Omega_c, \Omega_b, \sigma_8, h_0, n_s, w_0)$. The forward model can be found in `sbi_lens`.

We start by introducing our lensing forward modeling in Section 2. In Section 3 we introduce our Bayesian inference framework. Then in Section 4 we present the metric used to benchmark the different inference approaches. We then describe in Section 5 the explicit inference approach and present the results. It is followed by the implicit inference approaches both with and without gradients and the corresponding results in Section 6. Finally, we conclude in Section 7.

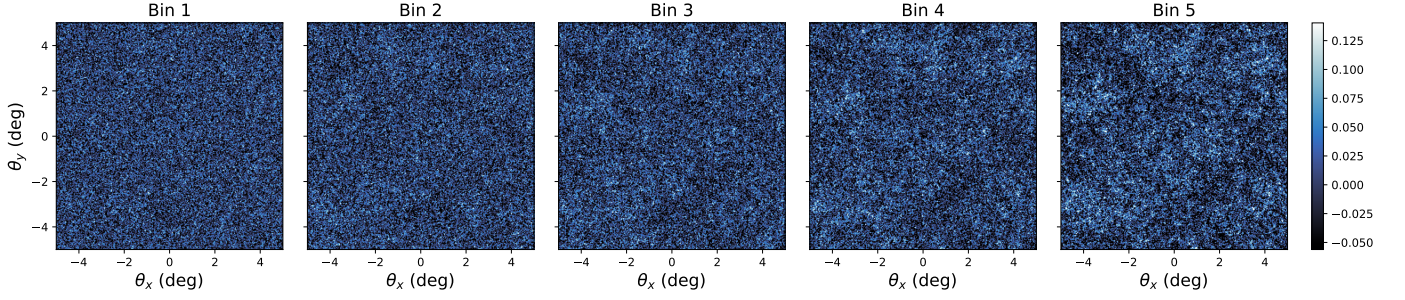


Fig. 1. Example of a noisy convergence map, with its five tomographic redshift bins, generating with `sbi_lens`'s log-normal forward model. It is the fiducial map x_0 used for benchmarking all the inference techniques.

2. The lensing forward model

Due to the non-linear growth of structures in the universe, the cosmological density field is expected to be highly non-Gaussian. Therefore log-normal fields which account for non-Gaussianities¹ provide a fast representation of the late-time 2D convergence field (Xavier et al. 2016a; Clerkin et al. 2017).

For our study, we use `sbi_lens`'s JAX-based differentiable forward model introduced in Lanzieri et al. (2024) to generate log-normal convergence maps at LSST Y10 quality. In this section, we recall the log-normal forward model of Lanzieri et al. (2024).

2.1. Log-Normal modeling

Given a Gaussian field κ_g fully characterized by its correlation function ξ_g^{ij} (i and j denoting the i -th and j -th source redshift bins see subsection 2.3) we parametrize the log-normal field κ_{ln} as

$$\kappa_{ln} = e^{\kappa_g} - \lambda, \quad (1)$$

with λ an additional parameter that makes the log-normal field more flexible than its corresponding Gaussian field. This parameter is called the "shift" or "minimum value" and depends on the cosmology. Hence, the field is no longer only described by its correlation function.

Note that this log-normal transformation leads to the following modification of the correlation function:

$$\xi_{ln}^{ij} = \lambda_i \lambda_j (e^{\xi_g^{ij}} - 1). \quad (2)$$

To ensure that the log-normal field shares the same correlation function as its Gaussian analog we apply the following correction

$$f(\xi^{ij}) = \log \left[\frac{\xi^{ij}}{\lambda_i \lambda_j} + 1 \right], \quad (3)$$

which also makes the correlation function independent of the choice of the shift parameter. However, the shift parameter has to be carefully set as it is related to the skewness of κ_{ln} . It can be computed from simulations using matching moments (Xavier et al. 2016b) or by using perturbation theory (Friedrich et al. 2020).

¹ Figure A.1 quantifies the amount of non-Gaussianities in our model compared to Gaussian simulations.

Finally, the correlation function is related to the power spectrum by

$$C_{ln}^{ij}(\ell) = 2\pi \int_0^\pi d\theta \sin \theta P_\ell(\cos \theta) \xi_{ln}^{ij}(\theta), \quad (4)$$

with P_ℓ the Legendre polynomial of order ℓ . In Fourier space, the covariance of κ_{ln} is diagonal and defined as:

$$\langle \hat{\kappa}_{ln}^{(i)}(\ell) \hat{\kappa}_{ln}^{*(j)}(\ell') \rangle = C_{ln}^{ij}(\ell) \delta^K(\ell - \ell'). \quad (5)$$

2.2. `sbi_lens`'s log-normal forward model

`sbi_lens`'s forward model is structured as follows (see Figure 2): first, we define the prior $p(\theta)$ over the cosmological parameters ($\Omega_c, \Omega_b, \sigma_8, n_s, w_0, h_0$) (see Table 1). Given a cosmology from the prior, we compute the corresponding nonlinear power spectrum $C_{\ell,g}$ using `JAX-COSMO` (Campagne et al. 2023a) that we project on two-dimensional grids of the size of the final mass map. For this cosmology, we also compute the cosmology-dependent shift parameter λ using `CosMomentum` (Friedrich et al. 2020). To ensure that the log-normal field preserves the power spectrum $C_{\ell,g}$ we apply the correction on the correlation function from Equation 3. Then, we convolve the Gaussian latent variables z (also known as *latent variables*) with the corrected two-dimensional power spectrum:

$$\hat{\kappa}_g = \hat{Z} \cdot \Sigma^{1/2}, \quad (6)$$

with \hat{Z} denoting the Fourier transform of the latent variables z and $\Sigma^{1/2}$ the square root of the covariance matrix

$$\Sigma = (C_{\ell}^{ij})_{1 \leq i \leq 4, 1 \leq j \leq 4}, \quad (7)$$

C_{ℓ}^{ij} denotes the corrected and projected nonlinear power spectrum. To compute the square root of the covariance matrix, we perform an eigenvalue decomposition of Σ :

$$\Sigma = Q \Lambda Q^T, \quad (8)$$

with Q the eigenvectors and Λ the eigenvalues of the symmetric matrix Σ . This allows us to compute the square root efficiently as

$$\Sigma^{1/2} = Q \Lambda^{1/2} Q^T. \quad (9)$$

Finally, we build the log-normal field κ_{ln} as described by Equation 1. An example of log-normal convergence maps is shown in Figure 1.

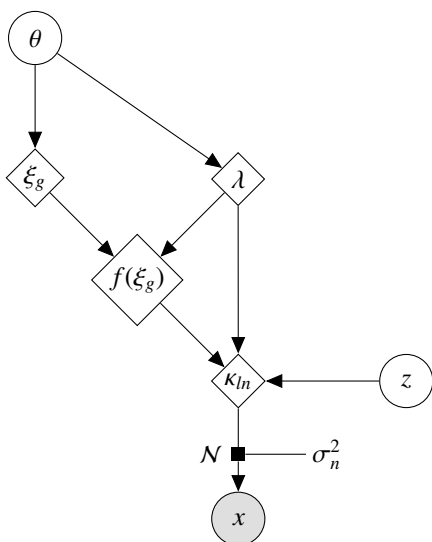


Fig. 2. Representation of the `sbi_lens`'s forward model used to generate log-normal convergence maps.

| Parameter | Prior | Fiducial value |
|------------|-------------------------------------------|----------------|
| Ω_c | $\mathcal{N}_{T[0,+\infty]}(0.2664, 0.2)$ | 0.2664 |
| Ω_b | $\mathcal{N}(0.0492, 0.006)$ | 0.0492 |
| σ_8 | $\mathcal{N}(0.831, 0.14)$ | 0.8310 |
| h_0 | $\mathcal{N}(0.6727, 0.063)$ | 0.6727 |
| n_s | $\mathcal{N}(0.9645, 0.08)$ | 0.9645 |
| w_0 | $\mathcal{N}_{T[-2.0,-0.3]}(-1.0, 0.9)$ | -1.0 |

Table 1. Prior $p(\theta)$ used in our forward model and fiducial values used for our inference benchmark. $\mathcal{N}_{T[low,high]}$ refers to truncated Normal distributions between *low* and *high*. The priors and fiducial values are the same as LSST DESC SRD.

2.3. LSST Y10 settings

According to the central limit theorem, we assume LSST Y10 observational noise to be Gaussian as we expect a high number of galaxies per pixel. Hence, the shear noise per pixel is given by zero-mean Gaussian whose standard deviation is

$$\sigma_n^2 = \frac{\sigma_e^2}{N_s}, \quad (10)$$

where $\sigma_e = 0.26$ is the per component shape standard deviation as defined in the LSST DESC Science Requirement Document (SRD, Mandelbaum et al. (2018)), and N_s is the number of source galaxies per bin and pixel, computed using $n_{gal} = 27 \text{ arcmin}^{-2}$ the galaxy number density (as in LSST DESC SRD) and $A_{pix} \approx 5.49 \text{ arcmin}^2$ the pixel area. The convergence field is related to the shear field through the Kaiser Squires operator (Kaiser & Squires 1993). As this operator is unitary, it preserves the noise of the shear field, therefore the convergence noise is also given by Equation 10.

Our convergence map, x , is a 256×256 pixels map that covers an area of $10 \times 10 \text{ deg}^2$ in five tomographic redshift bins with an equal number of galaxies (see Figure 3). The redshift distribution is modeled using the parametrized Smail distribution (Smail et al. 1995):

$$n(z) \propto z^2 \exp(-(z/z_0)^\alpha), \quad (11)$$

with $z_0 = 0.11$, $\alpha = 0.68$ and we assume a photometric redshift error $\sigma_z = 0.05(1+z)$ (still accordingly to LSST DESC SRD).

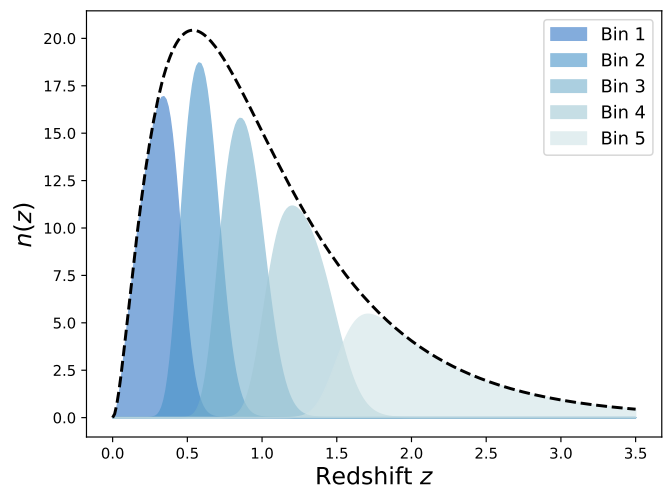


Fig. 3. LSST Y10 redshift distribution used in our forward model.

3. Bayesian Inference

In this section, we introduce our Bayesian inference framework enabling us to distinguish between implicit and explicit (full-field) inference more clearly in this paper.

Given a priori knowledge $p(\theta)$ about the parameters θ and information provided by data x linked to the parameters via the likelihood function $p(x|\theta)$, we are able to recover the parameters θ that might have led to this data. This is summarized by Bayes' theorem:

$$p(\theta|x) = \frac{p(x|\theta)p(\theta)}{p(x)}, \quad (12)$$

with $p(\theta|x)$ the posterior distribution of interest and $p(x) = \int p(x|\theta)p(\theta)d\theta$ the evidence. However, physical forward models are typically of the form $p(x|\theta, z)$ involving additional variables z known as latent variables. The presence of these latent variables make the link between the data x and the parameters θ not straightforward as x is now the result of a transformation involving two random variables θ and z . Since the forward model depends on latent variables, we need to compute the marginal likelihood to perform inference, i.e.

$$p(x|\theta) = \int p(x|\theta, z)p(z|\theta)dz, \quad (13)$$

which is typically intractable when z is of high dimension. As a result, the marginal likelihood $p(x|\theta)$ cannot be evaluated and explicit inference techniques that rely on explicit likelihood such as MCMC or variational inference cannot be directly applied on the marginal likelihood $p(x|\theta)$. For this reason, this marginal likelihood is often assumed to be Gaussian yielding to inaccurate estimation of the true posterior. Full-field inference instead aims to consider the exact distribution of the data x or the sufficient statistics t .

4. Inference quality evaluation

To quantify the quality of inference and thus benchmark all the inference algorithms, a performance metric has to be carefully chosen. Several metrics exist, each offering varying levels of precision, and are usually chosen according to the knowledge we have about the true posterior (i.e. if we have access to the probability density function of the true distributions, its samples, or only the fiducial data or fiducial parameters).

We choose to take the 160 000 posterior samples obtained through explicit full-field inference as our ground truth and use the Classifier 2-Sample Tests (C2ST, Lopez-Paz & Oquab 2018). This decision is based on the understanding that the explicit full-field approach, which relies on sampling schemes, should theoretically converge to the true posterior distribution within the limit of a large number of samples. The convergence analysis of the MCMC, along with the large number of samples (160 000), indicates that the explicit full-field inference posterior has converged. Additionally, we confirm this by visually comparing in Figure 4 the marginals of those fully converged samples obtained through explicit full-field inference (black) to the marginals of the posterior obtained through implicit inference (blue). Although we present implicit inference performed with only 1 000 simulations in Figure 4, it's worth noting that we ran the implicit inference method with over 1 000 simulations and it was consistently in agreement with this explicit posterior.

Since we are using samples from this explicit approach as our ground truth, 2-sample tests, specifically the C2ST is the most powerful metric to be used to compare two distributions (according to Lueckmann et al. (2021) benchmark). A two-sample test is a statistical method that tests whether samples $X \sim P$ and $Y \sim Q$ are sampled from the same distribution. For this, one can train a binary classifier f to discriminate between X (label 0) and Y (label 1) and then compute the C2ST statistic

$$\hat{t} = \frac{1}{N_{test}} \sum_{i=1}^{N_{test}} \mathbb{I} \left(\mathbb{I} \left(f(z_i) > \frac{1}{2} \right) = l_i \right), \quad (14)$$

where $\{(x_i, 0)\}_{i=1}^N \cup \{(y_i, 1)\}_{i=1}^N =: \{(z_i, l_i)\}_{i=1}^{2N}$ and N_{test} denotes the number of samples not used during the classifier training. If $P = Q$, the classifier fails to distinguish the two samples and thus the C2ST statistic remains at chance level (C2ST = 0.5). On the other hand, if P and Q are so different that the classifier perfectly matches the right label, C2ST = 1.

In practice, in our 6 dimensional inference problem, we find this metric very sensitive, and the two distributions considered converged in Figure 4 result in a C2ST of 0.6.

Therefore, to make a fair comparison between all inference methods we benchmark all the methods with the same metric, the C2ST metric, and choose to fix a threshold of 0.6.

5. Explicit inference

5.1. Sampling the forward model

When the forward model is explicit, which means that the joint likelihood $p(x|\theta, z)$ can be evaluated, it is possible to sample it directly through MCMC bypassing the computation of the intractable marginal likelihood $p(x|\theta)$.

Unlike sampling the marginal likelihood, this necessitates sampling both the parameters of interest θ as well as all latent variables z involved in the forward model:

$$p(\theta, z|x) \propto p(x|\theta, z) p(z|\theta) p(\theta), \quad (15)$$

and to marginalize over the latent variables z afterward to get the posterior distribution $p(\theta|x)$.

As the latent variables are usually high-dimensional they require a large number of sampling steps to make the MCMC converge. Therefore, Hamilton Monte Carlo (HMC, Neal et al. 2011; Betancourt 2018), which can efficiently explore the parameter space thanks to gradient information, is usually used for such high-dimensional posteriors. However, this requires the explicit likelihood to be differentiable.

Note that, for each step, the forward model needs to be called, which can make this approach costly in practice as generating one simulation can take a very long time. This would also be true in cases where the marginal likelihood can be evaluated but since the latent variables z do not have to be sampled, the parameter space is smaller and the MCMC does not need as many steps.

5.2. Explicit full-field inference constraints

`sbi_lens`' differentiable joint likelihood is:

$$p(x|\theta, z) = \mathcal{N}(\kappa_{ln}(\theta, z), \sigma_n^2), \quad (16)$$

with κ_{ln} the convergence map that depends on the cosmology θ and the latent variables z . Given that the observational noise is uncorrelated across tomographic redshift bins and pixels, we can express the log-likelihood of the observed data x_0 as:

$$\mathcal{L}(\theta, z) = constant - \sum_i^{N_{pix}} \sum_j^{N_{bins}} \frac{[\kappa_{ln}^{i,j}(\theta, z) - x_0^{i,j}]^2}{2\sigma_n^2}. \quad (17)$$

By construction $p(z|\theta)$ is independent of the cosmology θ , hence the log posterior we aim to sample is:

$$\log p(\theta, z|x = x_0) \propto \mathcal{L}(\theta, z) + \log p(z) + \log p(\theta), \quad (18)$$

with $p(z)$ a reduced centered Gaussian and $p(\theta)$ as in Table 1. We use a HMC scheme to sample Equation 18. Specifically, we use the No-U-Turn sampler (NUTS, Hoffman & Gelman 2011) from NumPyro (Phan et al. 2019; Bingham et al. 2019) that efficiently proposes new relevant samples using the derivatives of the distribution we sample from, namely: $\nabla_{\theta, z} \log p(\theta, z|x = x_0)$.

Given the fixed observed convergence map x_0 , Figure 4 shows the posterior constraints on $\Omega_c, \Omega_b, \sigma_8, n_s, w_0, h_0$. As explained in Section 4, we consider this posterior of 160 000 samples converged as it yields the same constraint as our implicit full-field approach. Therefore, we consider these 160 000 samples as our ground truth.

5.3. How many simulations for explicit full-field inference?

We now conduct a study to access the minimum number of simulations needed to get a good approximation of posterior distribution $p(\theta|x = x_0)$. In other words, we try to access the minimum number of simulations needed to have converged MCMC chains and a good representation of the posterior distribution.

Since there is no robust metric to estimate the convergence of MCMCs and because we aim to compare all inference methods with the same metric, we use the C2ST metric to access the minimum number of simulations required to have converged chains. We proceed as follows: given the fully converged chains of 160 000 posterior samples from Figure 4, for each number of simulation N , we take the first N samples and compute the C2ST metric comparing those samples to the 160 000 ones from the fully converged chains.

The C2ST metric is based on the training of a classifier to distinguish between two populations under the cross-entropy loss and thus requires an equal number of samples of the two distributions. We use a Kernel Density Estimator (KDE) (Parzen 1962) to fit the samples enabling us to generate the required number of samples to compare the two distributions. Note that KDEs, Gaussian filters, or smoothing are always used to visualize distribution samples using contour plots, thus motivating

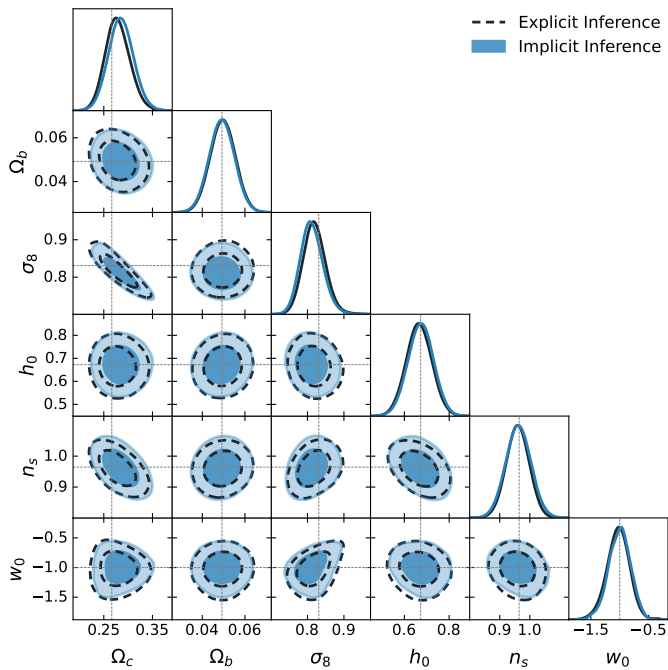


Fig. 4. From log-normal simulated convergence maps at LSST Y10 quality, we constrain the w CDM parameters using two approaches: 1) the explicit full-field inference (black), obtained by sampling 160 000 posterior samples through Hamilton Monte Carlo (HMC) scheme; 2) the implicit full-field inference contours (blue), obtained by compressing the convergence maps into sufficient statistics using Variation Mutual Information Maximisation (VMIM) and performing inference using NLE with 1 000 simulations. We show three things: 1) implicit and explicit full-field inference yield consistent constraints; 2) our implicit inference, when combined with an optimal compression procedure, allows full-field inference; 3) the C2ST metric indicates convergence when it is equal to 0.5 (see Section 4). However, when comparing explicit and implicit inference (which should theoretically yield the same posterior), we never reach this value but rather get 0.6. We justify that this value is acceptable and use it as a threshold for all benchmarked methods in this paper by showing that the marginals of the two approaches match, even though their C2ST is 0.6.

our approach. In addition, the distribution of interest is a 6 dimension unimodal and almost Gaussian distribution making it easy to fit through KDE. We use a Gaussian kernel and adjust the bandwidth to align with the contour plots shown by GetDist, as highlighted in Figure E.7.

Note that samples and simulations are not the same thing. During each step, the proposal of the MCMC suggests a pair of parameters θ_1 and z_1 and produces a corresponding simulation $x \sim p(x|\theta = \theta_1, z = z_1)$. The MCMC keeps only the parameters θ_1 and z_1 if it yields a plausible x according to the likelihood function evaluated on the observation x_0 , and plausible θ_1 and z_1 according to their priors. The sample is the pair θ and z that is kept by the MCMC. Specifically, to get one posterior sample using the NUTS algorithm we need $2 \times N$ simulations with N denoting the number of leapfrog steps. Indeed, the proposal of HMC methods is based on Hamiltonian equations which are discretized using the leapfrog integrator:

$$r^{t+\epsilon/2} = r^t - (\epsilon/2)\nabla_\alpha \log p(\alpha^t|x_0), \quad (19)$$

$$\alpha^{t+\epsilon} = \alpha^t + \epsilon M^{-1} r^{t+\epsilon/2}, \quad (20)$$

$$r^{t+\epsilon} = r^{t+\epsilon/2} - (\epsilon/2)\nabla_\alpha \log p(\alpha^{t+\epsilon}|x_0), \quad (21)$$

with ϵ the step size, M the mass matrix, α^t correspond to the position of (θ, z) at time t , and r^t denote the values of the random momentum at time $t \in [0, N]$. After N leapfrog steps, the total number of log probability evaluations is N . As each gradient requires the cost of two simulations (one to evaluate the primal values during the forward pass and one to evaluate gradients backward in the reverse mode of automatic differentiation), the total number of simulations is $2 \times N$. In our case, we find that the NUTS algorithm requires $2 \times (2^6 - 1) = 126$ simulations (always reaching the maximum depth of the tree which is set to 6) to generate one sample.

Figure 5 shows the convergence results of our explicit full-field inference as a function of the number of simulations and the effective sample size. According to the threshold of C2ST= 0.6 that we have chosen in Section 4, this study suggests that 630 000 simulations for our sampler corresponding to 400 independent samples are enough to have converged MCMC chains. The number of independent samples is estimated using the effective sample size (ess) lower bound estimate from TensorFlow Probability (Dillon et al. 2017). In addition, Figure E.6 shows the explicit posterior constraints obtained for different simulation budgets, and Figure E.5 shows the evolution of the mean and standard deviation of the posteriors as a number of simulations. Note that the C2ST metric is sensitive to higher-order correlations, but if one only cares about marginals, the explicit inference posterior can be considered converged with only 63 000 simulations (corresponding to 24 independent samples) as shown by the combination of contour plots Figure E.6 and Figure E.5.

These results are not a strong statement about explicit inference in general as we do not investigate other sampling schemes and preconditioning schemes (this study is left for future work). However, the NUTS algorithm is one of the state-of-the-art samplers and has already been used in various full-field studies (e.g. Zhou et al. 2023; Boruah et al. 2024). But it is important to note that there exist other powerful HMC schemes such as the Microcanonical Langevin Monte Carlo (MCLMC) (Robnik et al. 2023) that might perform with fewer simulations and has also been used in full-field studies (Bayer et al. 2023). Regardless of the sampling scheme used, we suggest that readers refer to the effective sample size values to translate the results to their sampler.

6. Implicit Inference

Although explicit full-field inference offers a promising framework for performing rigorous Bayesian inference it comes with the downside of requiring an explicit likelihood. Additionally, sampling from the joint likelihood even with HMC schemes can be very challenging and require a large number of simulations. Instead, implicit inference has emerged as a solution to tackle the inference problem without relying on having an explicit likelihood. These techniques rely on implicit likelihoods, more commonly known as simulators. A simulator is a stochastic process that takes as input the parameter space $\theta \sim p(\theta)$ and returns a random simulation x . It does not require the latent process of the simulator to be explicit.

Comparably to sampling the forward model, given an observation x_0 , to build the posterior $p(\theta|x = x_0)$, one can simulate a large range of θ_i and accept the parameters that verify $|x_i - x_0| < \epsilon$ with ϵ a fixed threshold. This is the idea behind Approximate Bayesian Computation (ABC) method (e.g. Rubin 1984; Beaumont et al. 2002; Sisson et al. 2018). This method used to be the traditional way to do implicit inference but its poor scalability with dimension encouraged the community to develop new

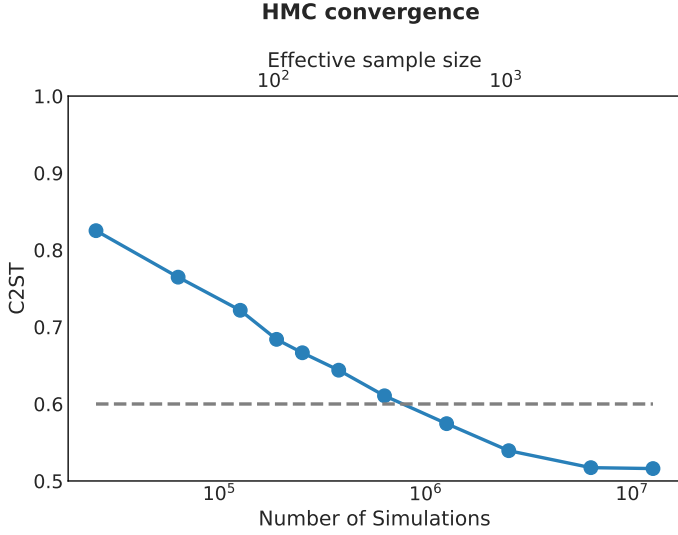


Fig. 5. Explicit full-field inference: quality of the cosmological posterior approximation as a function of the number of simulations used and effective sample size. The dashed line indicates the C2ST threshold of 0.6, marking the point at which the posterior is considered equal to the true distribution (see Section 4).

techniques. In particular, the introduction of machine learning leading to neural implicit inference methods has been shown to perform better. These neural-based methods cast the inference problem into an optimization task, where the goal is to find the set of parameters φ so that the neural parametric model best describes the data. Then, the posterior is approximated using this surrogate model evaluated on the given observation.

Implicit inference has already been successfully applied to cosmic shear analyses. For instance, Lin et al. (2023) and von Wietersheim-Kramsta et al. (2024) applied it to two-point statistics rather than using the standard explicit inference method assuming a Gaussian likelihood. Similarly, to bypass this traditional Gaussian likelihood assumption, Jeffrey et al. (2024) applied implicit inference to the power spectra, peak counts, and neural summary statistics.

In this section, we introduce the NLE method, its augmented version with gradient ∂ NLE, and we present the benchmark results. The Neural Ratio Estimation (NRE), and Neural Posterior Estimation (NPE) as well as sequential methods are described in subsection B.1 and the benchmark results of (S)NLE, (S)NPE and (S)NRE can be found in subsection B.3. In this section, we chose to focus our study on the NLE method as our comparison of the three main implicit inference methods (see Figure B.1) suggests that NLE and NPE are the ones that perform the best. We chose not to use the NPE method as the augmented gradient version of NPE (Zeghal et al. 2022) requires specific neural architectures that proved to be more simulation-costly.

6.1. Learning the Likelihood

Neural Likelihood Estimation (NLE) aims to learn the marginal likelihood $p_\varphi(x|\theta)$ from a set of parameters and corresponding simulations $(\theta, x)_{i=1..N}$. Thanks to the development of new architectures in the neural density estimator field, this can be achieved by using conditional Normalizing Flows (NFs) (Rezende & Mohamed 2015). Conditional NFs are parametric models p_φ that take as input (θ, x) and return a probability density $p_\varphi(x|\theta)$, which can be evaluated and/or sampled. To find the optimal parameters

$\hat{\varphi}$ which makes $p_\varphi(x|\theta)$ best describe the data, one trains the NF so that the approximate distribution $p_\varphi(x|\theta)$ is the closest to the unknown distribution $p(x|\theta)$. To quantify this, we use the forward Kullback–Leibler divergence $D_{KL}(\cdot \| \cdot)$. The D_{KL} is positive, and equal to zero if and only if the two distributions are the same, motivating the following optimization scheme:

$$\begin{aligned} \hat{\varphi} &= \arg \min_{\varphi} \mathbb{E}_{p(\theta)} \left[D_{KL}(p(x|\theta) \| p_\varphi(x|\theta)) \right] \\ &= \arg \min_{\varphi} \mathbb{E}_{p(\theta)} \left[\mathbb{E}_{p(x|\theta)} \left[\log \left(\frac{p(x|\theta)}{p_\varphi(x|\theta)} \right) \right] \right] \\ &= \arg \min_{\varphi} \underbrace{\mathbb{E}_{p(\theta)} \left[\mathbb{E}_{p(x|\theta)} \left[\log (p(x|\theta)) \right] \right]}_{\text{constant w.r.t } \varphi} \\ &\quad - \mathbb{E}_{p(\theta)} \left[\mathbb{E}_{p(x|\theta)} \left[\log (p_\varphi(x|\theta)) \right] \right] \\ &= \arg \min_{\varphi} -\mathbb{E}_{p(\theta)} \left[\mathbb{E}_{p(x|\theta)} \left[\log (p_\varphi(x|\theta)) \right] \right] \end{aligned} \quad (22)$$

leading to the loss

$$\mathcal{L} = \mathbb{E}_{p(\theta, x)} \left[-\log p_\varphi(x|\theta) \right], \quad (23)$$

which does not require evaluation of the true target distribution $p(x|\theta)$ anymore. To compute this loss, only a set of simulations $(\theta, x) \sim p(\theta, x)$ obtained by first generating parameters from the prior $\theta_i \sim p(\theta)$ and then generating the corresponding simulation $x_i \sim p(x|\theta = \theta_i)$ through the simulator, are needed. Note that the approximated likelihood, under the loss of Equation 23, is learned for every combination $(\theta, x) \sim p(x, \theta)$ at once.

Given observed data x_0 , the approximated posterior $\hat{p}(\theta|x = x_0) \propto p_\varphi(x = x_0|\theta)p(\theta)$ is then obtained by using an MCMC with the following log probability: $\log p_\varphi(x = x_0|\theta) + \log p(\theta)$. This MCMC step makes NLE (and NRE) less amortized and slower than the NPE method which directly learned the posterior distribution $p_\varphi(\theta|x)$ for every pair $(\theta, x) \sim p(x, \theta)$ and only need to be evaluated on the desire observation x_0 to get the approximated posterior $p_\varphi(\theta|x = x_0)$. However, it is less challenging than using an MCMC scheme to sample the forward model in the explicit inference framework. Indeed, now one only has to sample the learned marginal likelihood $p_\varphi(x|\theta)$ (or learned likelihood ratio) not the joint likelihood of the forward model $p(x|\theta, z)$.

6.2. NLE augmented with gradients

Although there are methods to reduce the number of simulations, such as sequential approaches (see Appendix B), they still treat the simulator as a black box. As underlined by Cranmer et al. (2020), the emergence of probabilistic programming languages makes it easier to open this black box (making the implicit likelihood explicit) and extract additional information such as the gradient of the simulation. In particular, Brehmer et al. (2020) noticed that they can compute the joint score $\nabla_\theta \log p(x, z|\theta)$ as the sum of the scores of all the latent transformations encounter in the differentiable simulator:

$$\begin{aligned} \nabla_\theta \log p(x, z|\theta) &= \nabla_\theta \log p(x|\theta, z) + \nabla_\theta \log p(z|\theta) \\ &= \nabla_\theta \log p(x|\theta, z) + \sum_i^N \nabla_\theta \log p(z_i|z_1 \dots z_{i-1}, \theta). \end{aligned} \quad (24)$$

The most important result: through the use of the classical mean squared error (MSE) loss (also known as score matching (SM) loss)

$$\mathcal{L}_{SM} = \mathbb{E}_{p(x, z, \theta)} \left[\|\nabla_\theta \log p(x, z|\theta) - \nabla_\theta \log p_\varphi(x|\theta)\|_2^2 \right], \quad (26)$$

they showed how to link this joint score to the intractable marginal score $\nabla_{\theta} \log p(x|\theta)$. As explained in [Appendix C](#), \mathcal{L}_{SM} is minimized by $\mathbb{E}_{p(z|x,\theta)} [\nabla_{\theta} \log p(x, z|\theta)]$ and can be derived as

$$\begin{aligned} & \mathbb{E}_{p(z|x,\theta)} [\nabla_{\theta} \log p(x, z|\theta)] \\ &= \mathbb{E}_{p(z|x,\theta)} [\nabla_{\theta} \log p(z|x, \theta)] + \nabla_{\theta} \log p(x|\theta) \\ &= \mathbb{E}_{p(z|x,\theta)} \left[\frac{\nabla_{\theta} p(z|x, \theta)}{p(z|x, \theta)} \right] + \nabla_{\theta} \log p(x|\theta) \\ &= \int \nabla_{\theta} p(z|x, \theta) dz + \nabla_{\theta} \log p(x|\theta) \\ &= \nabla_{\theta} \int p(z|x, \theta) dz + \nabla_{\theta} \log p(x|\theta) \\ &= \nabla_{\theta} \log p(x|\theta). \end{aligned} \quad (27)$$

This loss learns how the probability of x given θ changes according to θ and thus can be combined with the traditional negative log-likelihood loss ([Equation 13](#)) to help the neural density estimator learn the marginal likelihood with fewer simulations. The NF now learns $p_{\varphi}(x|\theta)$ from $(\theta, x, \nabla_{\theta} \log p(x, z|\theta))_{i=1..N}$ under the combined loss:

$$\mathcal{L} = \mathcal{L}_{NLL} + \lambda \mathcal{L}_{SM}, \quad (28)$$

with λ a hyper-parameter that has to be fined-tuned according to the task at hand. [Brehmer et al. \(2020\)](#) called this method SCORe-Augmented Neural Density Approximates Likelihood (SCAN-DAL) we choose to rename it ∂ NLE for clarity in our paper.

Equivalently, other quantities such as the joint likelihood ratio $r(x, z|\theta_0, \theta_1) = p(x, z|\theta_0)/p(x, z|\theta_1)$ and the joint posterior gradients $\nabla_{\theta} \log p(\theta|x, z)$ can be used to help learning the likelihood ratio ([Brehmer et al. 2020](#)) and the posterior ([Zeghal et al. 2022](#)) respectively.

6.3. Compression procedure

In this section, we provide a brief summary of the compression procedure we perform to build sufficient statistics. A more detailed description and comparison of compression procedures applied in the context of weak-lensing full-field implicit inference can be found in [Lanzieri et al. \(2024\)](#).

Based on the benchmark results of [Lanzieri et al. \(2024\)](#), we choose to use the Variational Mutual Information Maximisation (VMIM, [Jeffrey et al. 2021](#)) neural compression. This compression builds summary statistics $t = F_{\varphi}(x)$ by maximizing the mutual information $I(t, \theta)$ between the parameters of interest θ and the summary statistics t . More precisely, the mutual information is defined as

$$I(t, \theta) = \mathbb{E}_{p(t,\theta)} [\log p(\theta|t)] - H(\theta), \quad (29)$$

where H denotes the entropy. Replacing the summary statistics t by the neural network F_{φ} and the intractable posterior $p(\theta|t)$ by a variational distribution $p_{\psi}(\theta|t)$ to be optimized jointly with the compressor, we get the following variational lower bound ([Barber & Agakov 2003](#)):

$$I(t, \theta) \geq \mathbb{E}_{p(x,\theta)} [\log p_{\psi}(\theta | F_{\varphi}(x))] - H(\theta). \quad (30)$$

Hence, by training the neural network F_{φ} jointly with a variational distribution (typically a NF) p_{ψ} under the loss

$$\mathcal{L}_{VMIM} = -\mathbb{E}_{p(x,\theta)} [\log p_{\psi}(\theta | F_{\varphi}(x))], \quad (31)$$

enable, by construction and within the limit of the flexibility of F_{φ} and p_{ψ} , to build summary statistics t that contain the

maximum amount of information regarding θ that is embedded in the data x . As equality is approached, the maximization of the mutual information yields sufficient statistics such that $p(\theta|x) = p(\theta|t)$.

As proof that in our particular case, these summary statistics extract all the information embedded in our convergence maps, and thus are sufficient statistics, we show in [Figure 4](#) that the contours obtained using this compression and NLE implicit inference technique allow us to recover the explicit full-field constraints.

We used 100 000 simulations for the compression part and did not investigate the question of the minimum number of simulations required. Although we use a large number of simulations to train our compressor, we can produce near-optimal summary statistics without training a neural network, which eliminates the need for additional simulations. As an example, [Cheng et al. \(2020\)](#) shows that they can produce summary statistics using scattering transforms that result in constraints similar to those obtained by building summary statistics using a CNN trained under mean absolute error (MAE) loss. While it is not guaranteed that these scattering transform coefficients provide sufficient statistics required to perform full-field inference, we hope that advances in transfer learning will allow us to propose new compression schemes that need very few simulations. This is left for future work.

Details regarding our compressor architecture can be found in [subsection D.1](#).

6.4. Results

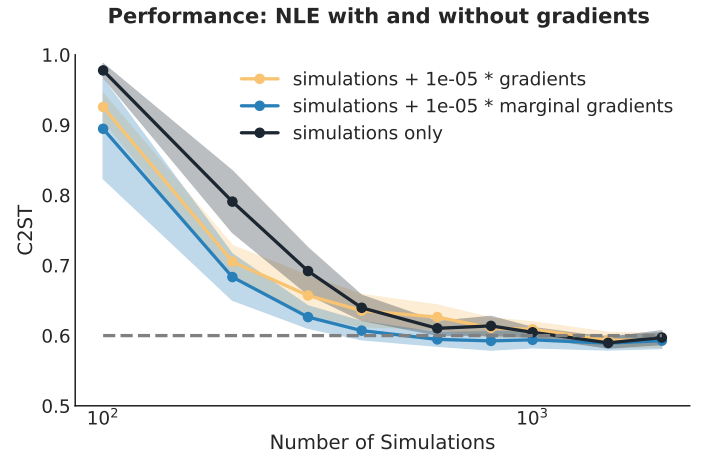


Fig. 6. Implicit inference augmented with gradients: quality of the cosmological posterior approximation as a function of the number of simulations used. We compare three methods: 1) ∂ NLE with the gradients of the simulator $\nabla_{\theta} \log p(x, z|\theta)$ (yellow); 2) ∂ NLE with marginal gradients $\nabla_{\theta} \log p(x|\theta)$ (blue); 3) the classical NLE method (black). The dashed line indicates the C2ST threshold of 0.6, marking the point at which the posterior is considered equal to the true distribution (see [Section 4](#)). We show that the gradients provided by the simulator (yellow curve) do not help to reduce the number of simulations as they are too noisy (see [Figure 7](#)).

For this study, we use the NLE algorithm as in [Papamakarios et al. \(2018b\)](#). And use the ∂ NLE method introduced by [Brehmer et al. \(2020\)](#) to leverage gradient information. All approaches share the same NF architecture and sampling scheme (all details can be found in [Appendix D subsection D.3](#)).

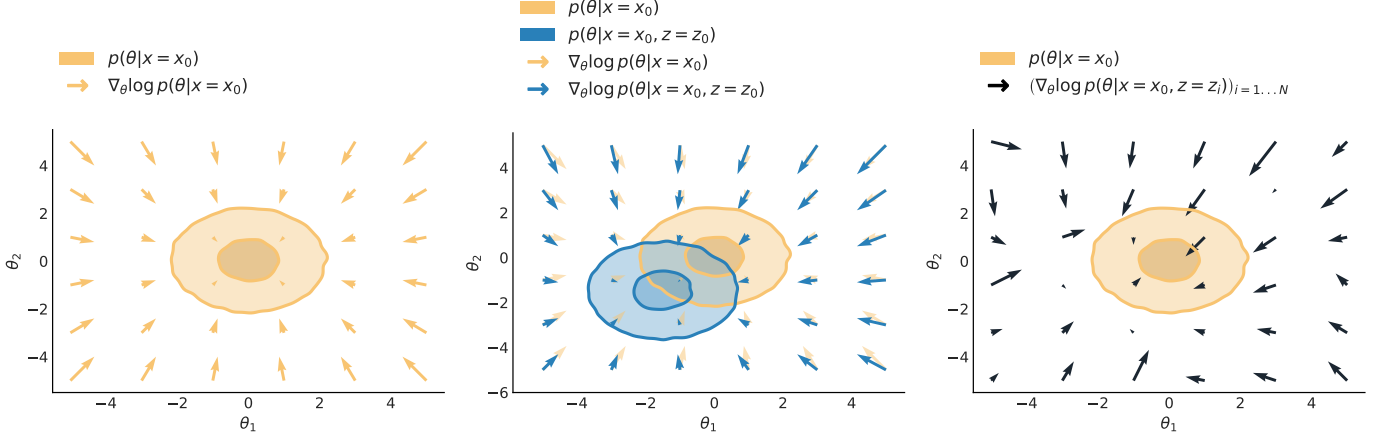


Fig. 7. Illustration of gradient stochasticity. The left panel shows a 2D posterior distribution $p(\theta|x = x_0)$ evaluated at the observed data x_0 and its gradients $\nabla_{\theta} \log p(\theta|x = x_0)$. The middle panel shows the difference between the posterior $p(\theta|x = x_0)$ (yellow) and the joint posterior $p(\theta|x = x_0, z = z_0)$ (blue) with z_0 a latent variable that leads to x_0 . The yellow arrows correspond to the gradients of the posterior, and the blue ones to the gradients of the joint posterior. The right panel displayed the gradients field that we obtained in practice from the simulator. Each gradient here aligns with its corresponding joint posterior resulting in a "noisy" gradient field compared to the gradient field of the posterior (first panel).

We benchmark the previously presented implicit inference methods on our `sbi_lens`'s log-normal LSST Y10-like forward model. The goal of this inference problem is to constrain the following cosmological parameters: $\Omega_c, \Omega_b, \sigma_8, n_s, w_0, h_0$ given a fiducial convergence map x_0 . Our fiducial map x_0 is the same for all the benchmarked methods in the paper.

This benchmark aims to find the inference method that can achieve a given posterior quality (C2ST = 0.6) with the minimum number of simulations, for this the procedure is the following:

1. Starting from the entire dataset, we compress the tomographic convergence maps x of $256 \times 256 \times 5$ pixels into 6-dimension sufficient statistics. We use the VMIM neural compression as described in [subsection 6.3](#).
2. From this compressed dataset, we then pick a number of simulations and approximate the posterior distribution using NLE and ∂ NLE methods.
3. Then we evaluate the approximated posterior against the fully converged explicit full-field posterior (our ground truth) using the C2ST metric.

The C2ST convergence results are displayed in [Figure 6](#). In Appendix we provide additional convergence results, [Figure E.1](#) shows the posterior contours evolution obtained through NLE and [Figure E.2](#), [Figure E.3](#), [Figure E.4](#) depicts the evolution of the mean and standard deviation of the approximated posterior as a number of simulation.

We find that unlike previous results ([Brehmer et al. 2020](#); [Zeghal et al. 2022](#)), the gradients $\nabla_{\theta} \log p(x, z|\theta)$ do not provide additional information enabling a reduction in the number of simulations. Indeed, [Figure 6](#) shows similar convergence curves for the ∂ NLE method (yellow) and NLE method (black). This issue arises as we attempt to constrain the gradients of the learned marginal distribution $p_{\varphi}(x|\theta)$ by using the joint gradients $\nabla_{\theta} \log p(x, z|\theta)$ from the simulator. Indeed, the benefit of these joint gradients depends on their "level of noise". In other words, their benefit depends on how much they vary compared to the marginal gradients. To visually exhibit this gradient stochasticity, we consider the gradients of a 2 dimensional posterior $\nabla_{\theta} \log p(\theta|x)$ and the joint gradients $\nabla_{\theta} \log p(\theta|x, z)$ provided by the simulator. By definition, the gradients should align with the

distribution, as seen in the left panel of [Figure 7](#). As demonstrated in the middle panel of [Figure 7](#), the gradients we obtain from the simulator are directed towards $p(\theta|x, z)$, which differs from $p(\theta|x) = \int p(\theta|x, z)p(z|x)dz$. The stochasticity of the gradients relies on the standard deviation of $p(z|x)$ and how much $p(\theta|x, z)$ "moves" according to z . As a result, instead of the gradients field being displayed in the left panel of [Figure 7](#), we end up with the gradients field depicted in the right panel.

To confirm this claim, we learn from the simulator's gradients $\nabla_{\theta} \log p(x, z|\theta)$ the marginal ones $\nabla_{\theta} \log p(x|\theta)$. For this, we use a neural network (the architecture can be found in [Appendix D subsection D.2](#)) that we train under the following MSE loss function:

$$\mathcal{L}_{\text{MarginalSM}} = \mathbb{E}_{p(x, z, \theta)} \left[\left\| \nabla_{\theta} \log p(x, z|\theta) - g_{\varphi}(x, \theta) \right\|_2^2 \right]. \quad (32)$$

This loss is almost the same as [Equation 26](#) except that instead of using a NF to approximate $\nabla_{\theta} \log p(x|\theta)$ and then take its gradients, we train a neural network to approximate the gradients values given θ and x . This loss is minimized by $g_{\varphi}(x, \theta) = \nabla_{\theta} \log p(x|\theta)$ (as explained in [subsection 6.2](#)) allowing us to learn the intractable marginal gradients from simulations.

We then use these marginal gradients in the ∂ NLE method (blue curve) and show that those gradients help to reduce the number of simulations.

What we have demonstrated here is that the stochasticity of our LSST Y10-like simulator dominates the gradient information and thus ∂ NLE method does not help to perform inference with fewer simulations.

We could have used a method to denoise the gradients. Specifically, [Millea & Seljak \(2022\)](#) introduced Marginal Unbiased Score Expansion (MUSE), a way of computing marginal gradients from simulations, and proposed a frequentist and Bayesian approach for parameter inference that leverages this quantity. In our case, the ∂ NLE with marginal gradients converges with ~ 400 simulations while ∂ NLE with gradients from the simulator converges with 2 times more simulations. Hence, to be beneficial, computing marginal gradient should take less than 2 simulations which is not feasible with MUSE as it requires at least 10 simulations to have an "acceptable" estimation of the marginal gradient ([Millea & Seljak 2022](#)).

7. Conclusion and Discussion

Full-field inference is the optimal form of inference as it aims to perform inference without any loss of information. This kind of inference is based on a simulation model known as a simulator, forward model, or Bayesian hierarchical model in cases where the model is hierarchical. There are two ways of conducting full-field inference from this forward model: through explicit or implicit inference. The first way can be applied when the forward model is explicit. This means that the field-based joint likelihood $p(x = x_0|\theta, z)$ can be evaluated and thus sampled through sampling schemes such as MCMC. The second one can be used when only simulations are available, in this case, it is said that the likelihood is implicit. While it is possible to perform implicit inference directly at the pixel level by feeding the maps to the neural density estimator (Dai & Seljak 2024), it is usually more robust and careful to decompose it into two steps: first performing a lossless compression and then performing the implicit inference on this sufficient statistics. Specifically, in this work, sufficient statistics are built using an optimal neural-based compression based on the maximization of the mutual information $I(\theta, t)$ between the cosmological parameters θ and the summary statistics t . But other compression schemes, requiring fewer or zero simulations, could be used while still offering very good quality summary statistics (Cheng et al. 2020). Additionally, the advent of transfer learning could offer a way for performing compression with fewer simulations; this is left for future work.

This work aimed to answer the following questions: which full-field inference methods require the minimum number of simulations? Is differentiability useful for implicit full-field inference?

To answer these questions, we have introduced a benchmark that compares various methods to perform weak lensing full-field inference. For our benchmark, we used `sbi_lens`'s differentiable forward model, which can generate log-normal convergence maps at the quality expected for the tenth year of LSST. We evaluated the performance of several inference strategies by evaluating the constraints on $(\Omega_c, \Omega_b, \sigma_8, h_0, n_s, w_0)$, specifically using the C2ST metric.

We found the following results:

1. Explicit and implicit full-field inference yield the same constraints. However, according to the C2ST metric and the threshold of $C2ST = 0.6$, the explicit full-field inference requires 630 000 simulations (corresponding to 400 independent samples). In contrast, the implicit inference approach requires 101 000 simulations split into 100 000 simulations for compression and 1 000 for inference. Note that we arbitrarily used 100 000 simulations for the compression part and did not explore the question of performing compression with a minimum number of simulations. Hence, 101 000 simulations is an upper bound of the number of simulations actually required to perform implicit full-field inference in this particular problem.
2. The C2ST is sensitive to higher-order correlations that one can not see by looking at the marginals or first moments making it a good metric for comparing distributions. However, as we mostly care about those marginals, it is worth noting that by looking at the combination of contour plots from Figure E.6 and first moments convergence plots from Figure E.5, the explicit inference can be considered "converged" with 63 000 simulations (corresponding to 24 independent samples) as emphasized by Figure E.6 which correspond to $C2ST=0.76$ and the implicit inference performed through NLE with 101 000 (1 000 for inference and 100 000

to build sufficient statistics) as shown in Figure 4 which corresponds to $C2ST=0.6$.

3. For implicit inference, we exploited the simulator's gradient using the SCANDAL method proposed by Brehmer et al. (2020). Our study indicates that the gradients contain a significant noise level due to the latent variable's behavior, which makes it difficult to achieve convergence with fewer simulations. Note that the effectiveness of such gradient-based methods depends on the specific problem at hand. These methods can still be useful in scenarios where the noise level is not significant. This has been demonstrated in studies such as Brehmer et al. (2020) and Zeghal et al. (2022). It is also important to keep in mind that there may be other ways to leverage the differentiability of simulators and encourage further research in this area. Finally, note that methods to denoise the gradients exist (Millea & Seljak 2022) but, in our specific case, the gain compared to the number of simulations that this method requires is not significant.

It is worth noting that for each explicit inference simulation budget, the C2ST is calculated against fully converged explicit inference samples, resulting in a value that can reach almost 0.5. For implicit inference, the C2ST is also computed against the fully converged explicit inference samples. Both methods should produce the same constraints, but due to slight differences in the posterior approximation, the C2ST cannot go below 0.6. Hence, we consider a value of 0.6 as indicating convergence (see Figure 4).

It is important to mention that in most of real-world physical inference problems, such a metric cannot be used as it requires comparing the approximated posterior to the true one. Instead, for implicit inference, coverage tests (Lemos et al. 2023) should be used to assess the quality of the posterior. For explicit full-field inference, although diagnostics exist it is very difficult to verify if the MCMC has explored the entire space. If possible, the safest would be comparing the two full-field approaches as they should yield the same posterior. Implicit inference is likely the easiest to use in such a scenario because it does not require modeling the very complicated latent process of the forward model and can be performed even in multimodal regimes. Whereas, explicit inference has to sample the latent process of the forward model and the more dimensions there are, the more time it needs to explore the entire parameter space. In addition, it can fail in the case of multimodal distribution as it can stay stuck in local maxima and never converge. However, for implicit inference, too few simulations can result in an overconfident posterior approximation, as shown in Figure E.1. Therefore, within the limit of a reasonable number of simulations, the implicit inference method should be the easiest to use.

Finally, we discuss some limitations of our setting. We chose to use a fast log-normal model that enables us to investigate various approaches for this benchmark. While this model takes into account additional non-Gaussianity (as illustrated in Figure A.1), it is not as realistic as expensive N-Body simulations. Moreover, we did not include any systematics. However, we are optimistic that our findings will be relevant for realistic weak lensing inference. Additionally, even though these numerical results depend on our particular inference problem, we do not expect our conclusion regarding the comparison of implicit and explicit inference, to change when using a more realistic gravity model but it will be interesting to confirm this in future work.

The explicit inference results are not a strong statement, as we did not explore other sampling and preconditioning schemes

(which is left for future work). Our sampler choice for the benchmark has been motivated by the fact that the NUTS algorithm is a state-of-the-art sampler and has been extensively used in full-field studies (Zhou et al. 2023; Boruah et al. 2024). But there exist other sampling schemes such as powerful Microcanonical Langevin Monte Carlo (MCLMC) (Robnik et al. 2023) that might require fewer simulations and have been applied in full-field studies (Bayer et al. 2023). Meanwhile, we recommend the reader refer to the effective sample size values to translate the results to its sampler.

We use the NLE implicit method for our study as, regarding our benchmark results of Figure B.1, it seems to be the one that performs the best. NPE provides comparable results but necessitates using the ∂ NPE method of Zeghal et al. (2022) to leverage gradient information. Since the NPE method aims to learn the posterior directly, this method requires the NF to be differentiable. But, the smooth NF architecture (Köhler et al. 2021) that Zeghal et al. (2022) used was too simulation-expensive for our needs. We also experimented with continuous normalizing flows trained under negative log-likelihood loss but found that it took a very long time to train.

Acknowledgements. This paper has undergone internal review in the LSST Dark Energy Science Collaboration. The authors would like to express their sincere gratitude to the internal reviewers, Alan Heavens and Adrian Bayer, for their valuable feedback, insightful comments, and suggestions, which helped to significantly improve the quality of this work. They also extend their thanks to Benjamin Remy for his contributions through countless discussions and helpful comments on the paper. Additionally, they appreciate the constructive feedback provided by Martin Kilbinger and Sacha Guerrini. JZ led the project, contributed to brainstorming, developed the code, and wrote the paper. DL contributed to brainstorming and code development, particularly in developing the forward model, and reviewed the paper. FL initiated the project and contributed through mentoring, brainstorming, code development, and paper reviews. AB contributed mentoring, brainstorming, code development, and paper reviews. GL and EA provided mentoring, participated in brainstorming, and contributed to reviewing the paper. AB contributed to the review of the paper and participated in brainstorming the metric used for explicit inference. The DESC acknowledges ongoing support from the Institut National de Physique Nucléaire et de Physique des Particules in France; the Science & Technology Facilities Council in the United Kingdom; and the Department of Energy, the National Science Foundation, and the LSST Corporation in the United States. DESC uses resources of the IN2P3 Computing Center (CC-IN2P3-Lyon/Villeurbanne - France) funded by the Centre National de la Recherche Scientifique; the National Energy Research Scientific Computing Center, a DOE Office of Science User Facility supported by the Office of Science of the U.S. Department of Energy under Contract No. DE-AC02-05CH11231; STFC DiRAC HPC Facilities, funded by UK BEIS National E-infrastructure capital grants; and the UK particle physics grid, supported by the GridPP Collaboration. This work was performed in part under DOE Contract DE-AC02-76SF00515. This work was supported by the Data Intelligence Institute of Paris (diiP), and IdEx Université de Paris (ANR-18-IDEX-0001). This work was granted access to the HPC/AI resources of IDRIS under the allocations 2023-AD010414029 and AD011014029R1 made by GENCI. This work used the following packages: Numpy (Harris et al. 2020), NumPyro (Phan et al. 2019), JAX (Bradbury et al. 2018), Haiku (Hennigan et al. 2020), Optax (DeepMind et al. 2020), JAX-COSMO (Campagne et al. 2023b), GetDist (Lewis 2019), Matplotlib (Hunter 2007), CosMomentum (Friedrich et al. 2020), scikit-learn (Pedregosa et al. 2011), TensorFlow (Abadi et al. 2015), TensorFlow Probability (Dillon et al. 2017), sbi (Tejero-Cantero et al. 2020) and sbibm (Lueckmann et al. 2021).

References

Abadi, M., Agarwal, A., Barham, P., et al. 2015, TensorFlow: Large-Scale Machine Learning on Heterogeneous Systems, software available from tensorflow.org
 Aihara, H., Arimoto, N., Armstrong, R., et al. 2017, Publications of the Astronomical Society of Japan, 70
 Ajani, V., Peel, A., Pettorino, V., et al. 2020, Physical Review D, 102, 103531
 Akhmetzhanova, A., Mishra-Sharma, S., & Dvorkin, C. 2024, MNRAS, 527, 7459

Alsing, J., Heavens, A., & Jaffe, A. H. 2017, Monthly Notices of the Royal Astronomical Society, 466, 3272
 Alsing, J., Heavens, A., Jaffe, A. H., et al. 2016, Monthly Notices of the Royal Astronomical Society, 455, 4452
 Barber, D. & Agakov, F. 2003, Advances in Neural Information Processing Systems, 16
 Bayer, A. E., Seljak, U., & Modi, C. 2023, Field-Level Inference with Microcanonical Langevin Monte Carlo
 Beaumont, M. A., Zhang, W., & Balding, D. J. 2002, Genetics, 162, 2025
 Betancourt, M. 2018, A Conceptual Introduction to Hamiltonian Monte Carlo
 Bingham, E., Chen, J. P., Jankowiak, M., et al. 2019, J. Mach. Learn. Res., 20, 28:1
 Blum, M. G. B. & François, O. 2009, Statistics and Computing, 20, 63
 Böhm, V., Hilbert, S., Greiner, M., & Enßlin, T. A. 2017, Physical Review D, 96, 123510
 Boruah, S. S., Fiedorowicz, P., & Rozo, E. 2024, Bayesian mass mapping with weak lensing data using KARMMA – validation with simulations and application to Dark Energy Survey Year 3 data
 Bradbury, J., Frostig, R., Hawkins, P., et al. 2018, JAX: composable transformations of Python+NumPy programs
 Brehmer, J., Louppe, G., Pavez, J., & Cranmer, K. 2020, Proceedings of the National Academy of Sciences, 117, 5242
 Campagne, J.-E., Lanusse, F., Zuntz, J., et al. 2023a, The Open Journal of Astrophysics, 6
 Campagne, J.-E., Lanusse, F., Zuntz, J., et al. 2023b, The Open Journal of Astrophysics, 6
 Charnock, T., Lavaux, G., & Wandelt, B. D. 2018, Physical Review D, 97
 Cheng, S., Ting, Y.-S., Ménard, B., & Bruna, J. 2020, Monthly Notices of the Royal Astronomical Society, 499, 5902
 Clerkin, L., Kirk, D., Manera, M., et al. 2017, Monthly Notices of the Royal Astronomical Society, 466, 1444
 Cranmer, K., Brehmer, J., & Louppe, G. 2020, Proceedings of the National Academy of Sciences, 117, 30055
 Cranmer, K., Pavez, J., & Louppe, G. 2015, Approximating Likelihood Ratios with Calibrated Discriminative Classifiers
 Dai, B. & Seljak, U. 2024, Multiscale Flow for Robust and Optimal Cosmological Analysis
 de Jong, J. T. A., Kleijn, G. A. V., Kuijken, K. H., & Valentijn, E. A. 2012, Experimental Astronomy, 35, 25
 DeepMind, Babuschkin, I., Baumli, K., et al. 2020, The DeepMind JAX Ecosystem
 Deistler, M., Goncalves, P. J., & Macke, J. H. 2022, Truncated proposals for scalable and hassle-free simulation-based inference
 Dillon, J. V., Langmore, I., Tran, D., et al. 2017, TensorFlow Distributions
 Dinh, L., Sohl-Dickstein, J., & Bengio, S. 2017, Density estimation using Real NVP
 Durkan, C., Murray, I., & Papamakarios, G. 2020, On Contrastive Learning for Likelihood-free Inference
 Erben, T., Hildebrandt, H., Miller, L., et al. 2013, Monthly Notices of the Royal Astronomical Society, 433, 2545
 Flaugher, B. 2005, International Journal of Modern Physics A, 20, 3121
 Fluri, J., Kacprzak, T., Lucchi, A., et al. 2022, Physical Review D, 105, 083518
 Fluri, J., Kacprzak, T., Refregier, A., et al. 2018, Phys. Rev. D, 98, 123518
 Friedrich, O., Uhlemann, C., Villaescusa-Navarro, F., et al. 2020, Monthly Notices of the Royal Astronomical Society, 498, 464
 Fu, L., Kilbinger, M., Erben, T., et al. 2014, Monthly Notices of the Royal Astronomical Society, 441, 2725
 Glöckler, M., Deistler, M., & Macke, J. H. 2022, Variational methods for simulation-based inference
 Greenberg, D. S., Nonnenmacher, M., & Macke, J. H. 2019, Automatic Posterior Transformation for Likelihood-Free Inference
 Gupta, A., Matilla, J. M. Z., Hsu, D., et al. 2018, 97, 103515
 Halder, A., Friedrich, O., Seitz, S., & Varga, T. N. 2021, Monthly Notices of the Royal Astronomical Society, 506, 2780
 Harnois-Déraps, J., Martinet, N., & Reischke, R. 2021, Monthly Notices of the Royal Astronomical Society
 Harris, C. R., Millman, K. J., van der Walt, S. J., et al. 2020, Nature, 585, 357
 He, K., Zhang, X., Ren, S., & Sun, J. 2015, Deep Residual Learning for Image Recognition
 Hennigan, T., Cai, T., Norman, T., Martens, L., & Babuschkin, I. 2020, Haiku: Sonnet for JAX
 Hermans, J., Begy, V., & Louppe, G. 2020, Likelihood-free MCMC with Amortized Approximate Ratio Estimators
 Hoffman, M. D. & Gelman, A. 2011, The No-U-Turn Sampler: Adaptively Setting Path Lengths in Hamiltonian Monte Carlo
 Hunter, J. D. 2007, Computing in Science & Engineering, 9, 90
 Ivezić, Ž., Kahn, S. M., Tyson, J. A., et al. 2019, The Astrophysical Journal, 873, 111
 Izbicki, R., Lee, A. B., & Schafer, C. M. 2014

- Jeffrey, N., Alsing, J., & Lanusse, F. 2021, *Monthly Notices of the Royal Astronomical Society*, 501, 954
- Jeffrey, N., Whiteway, L., Gatti, M., et al. 2024, arXiv e-prints, arXiv:2403.02314
- Jeffrey, N., Whiteway, L., Gatti, M., et al. 2024, Dark Energy Survey Year 3 results: likelihood-free, simulation-based Λ CDM inference with neural compression of weak-lensing map statistics
- Junzhe Zhou, A., Li, X., Dodelson, S., & Mandelbaum, R. 2023, arXiv e-prints, arXiv:2312.08934
- Kacprzak, T., Kirk, D., Friedrich, O., et al. 2016, *Monthly Notices of the Royal Astronomical Society*, 463, 3653
- Kaiser, N. & Squires, G. 1993, *Astrophysical Journal*, Part 1 (ISSN 0004-637X), vol. 404, no. 2, p. 441-450., 404, 441
- Kilbinger, M. 2015, *Reports on Progress in Physics*, 78, 086901
- Köhler, J., Krämer, A., & Noé, F. 2021, *Smooth Normalizing Flows*
- Lanzieri, D., Zeghal, J., Makinen, T. L., et al. 2024, Optimal Neural Summarisation for Full-Field Weak Lensing Cosmological Implicit Inference
- Laureijs, R., Amiaux, J., Arduini, S., et al. 2011, arXiv preprint arXiv:1110.3193
- Lemos, P., Coogan, A., Hezaveh, Y., & Perreault-Levasseur, L. 2023, *Sampling-Based Accuracy Testing of Posterior Estimators for General Inference*
- Lewis, A. 2019, *GetDist: a Python package for analysing Monte Carlo samples*
- Lin, C.-A. & Kilbinger, M. 2015, *Astronomy & Astrophysics*, 583, A70
- Lin, K., von Wietersheim Kramsta, M., Joachimi, B., & Feeney, S. 2023, *Monthly Notices of the Royal Astronomical Society*, 524, 6167–6180
- Liu, J., Petri, A., Haiman, Z., et al. 2015a, *Physical Review D*, 91, 063507
- Liu, X., Pan, C., Li, R., et al. 2015b, *Monthly Notices of the Royal Astronomical Society*, 450, 2888
- Lopez-Paz, D. & Oquab, M. 2018, *Revisiting Classifier Two-Sample Tests*
- Lueckmann, J.-M., Bassetto, G., Karaletsos, T., & Macke, J. H. 2018
- Lueckmann, J.-M., Boelts, J., Greenberg, D., Goncalves, P., & Macke, J. 2021, in *Proceedings of Machine Learning Research*, Vol. 130, *Proceedings of The 24th International Conference on Artificial Intelligence and Statistics*, ed. A. Banerjee & K. Fukumizu (PMLR), 343–351
- Lueckmann, J.-M., Goncalves, P. J., Bassetto, G., et al. 2017, *Flexible statistical inference for mechanistic models of neural dynamics*
- Mandelbaum, R., Eifler, T., Hložek, R., et al. 2018, arXiv preprint arXiv:1809.01669
- Martinet, N., Schneider, P., Hildebrandt, H., et al. 2018, *Monthly Notices of the Royal Astronomical Society*, 474, 712
- Millea, M. & Seljak, U. 2022, *Physical Review D*, 105
- Miller, B. K., Weniger, C., & Forré, P. 2023, *Contrastive Neural Ratio Estimation*
- Neal, R. M. et al. 2011, *Handbook of markov chain monte carlo*, 2, 2
- Papamakarios, G. & Murray, I. 2018, *Fast ϵ -free Inference of Simulation Models with Bayesian Conditional Density Estimation*
- Papamakarios, G., Pavlakou, T., & Murray, I. 2018a, *Masked Autoregressive Flow for Density Estimation*
- Papamakarios, G., Sterratt, D. C., & Murray, I. 2018b, *Sequential Neural Likelihood: Fast Likelihood-free Inference with Autoregressive Flows*
- Parzen, E. 1962, *The Annals of Mathematical Statistics*, 33, 1065
- Pedregosa, F., Varoquaux, G., Gramfort, A., et al. 2011, *Journal of Machine Learning Research*, 12, 2825
- Peel, A., Lin, C.-A., Lanusse, F., et al. 2017, *Astronomy & Astrophysics*, 599, A79
- Phan, D., Pradhan, N., & Jankowiak, M. 2019, *Composable Effects for Flexible and Accelerated Probabilistic Programming in NumPyro*
- Porqueres, N., Heavens, A., Mortlock, D., & Lavaux, G. 2021, *Monthly Notices of the Royal Astronomical Society*, 502, 3035
- Porqueres, N., Heavens, A., Mortlock, D., & Lavaux, G. 2022, *Monthly Notices of the Royal Astronomical Society*, 509, 3194
- Porqueres, N., Heavens, A., Mortlock, D., Lavaux, G., & Makinen, T. L. 2023, arXiv preprint arXiv:2304.04785
- Remy, B. 2023, PhD thesis, thèse de doctorat dirigée par Starck, Jean-Luc et Lanusse, Francois *Astronomie et Astrophysique université Paris-Saclay 2023*
- Rezende, D. J. & Mohamed, S. 2015, *Variational Inference with Normalizing Flows*
- Ribli, D., Pataki, B. Á., Zorrilla Matilla, J. M., et al. 2019, *Monthly Notices of the Royal Astronomical Society*, 490, 1843
- Rizzato, M., Benabed, K., Bernardeau, F., & Lacasa, F. 2019, *Monthly Notices of the Royal Astronomical Society*, 490, 4688
- Robnik, J., Luca, G. B. D., Silverstein, E., & Seljak, U. 2023, *Microcanonical Hamiltonian Monte Carlo*
- Rubin, D. B. 1984, *The Annals of Statistics*, 12, 1151
- Schneider, M. D., Hogg, D. W., Marshall, P. J., et al. 2015, *The Astrophysical Journal*, 807, 87
- Semboloni, E., Schrabback, T., van Waerbeke, L., et al. 2011, *Monthly Notices of the Royal Astronomical Society*, 410, 143
- Shan, H., Liu, X., Hildebrandt, H., et al. 2018, *Monthly Notices of the Royal Astronomical Society*, 474, 1116
- Sharrock, L., Simons, J., Liu, S., & Beaumont, M. 2022, *Sequential Neural Score Estimation: Likelihood-Free Inference with Conditional Score Based Diffusion Models*
- Sisson, S. A., Fan, Y., & Beaumont, M. A. 2018, *Overview of Approximate Bayesian Computation*
- Smail, I., Hogg, D. W., Yan, L., & Cohen, J. G. 1995, *The Astrophysical Journal*, 449, L105
- Spergel, D., Gehrels, N., Baltay, C., et al. 2015, arXiv preprint arXiv:1503.03757
- Takada, M. & Jain, B. 2004, *Monthly Notices of the Royal Astronomical Society*, 348, 897
- Tejero-Cantero, A., Boelts, J., Deistler, M., et al. 2020, *Journal of Open Source Software*, 5, 2505
- Thomas, O., Dutta, R., Corander, J., Kaski, S., & Gutmann, M. U. 2016, *Likelihood-free inference by ratio estimation*
- von Wietersheim-Kramsta, M., Lin, K., Tessore, N., et al. 2024, *KiDS-SBI: Simulation-Based Inference Analysis of KiDS-1000 Cosmic Shear*
- Wildberger, J. B., Dax, M., Buchholz, S., et al. 2023, in *ICML 2023 Workshop on Structured Probabilistic Inference & Generative Modeling*
- Wiqvist, S., Frellsen, J., & Picchini, U. 2021, *Sequential Neural Posterior and Likelihood Approximation*
- Wood, S. N. 2010, *Nature*, 466, 1102
- Xavier, H. S., Abdalla, F. B., & Joachimi, B. 2016a, *Monthly Notices of the Royal Astronomical Society*, 459, 3693
- Xavier, H. S., Abdalla, F. B., & Joachimi, B. 2016b, *Monthly Notices of the Royal Astronomical Society*, 459, 3693–3710
- Zeghal, J., Lanusse, F., Boucaud, A., Remy, B., & Aubourg, E. 2022, *Neural Posterior Estimation with Differentiable Simulators*
- Zhou, A. J., Li, X., Dodelson, S., & Mandelbaum, R. 2023, *Accurate field-level weak lensing inference for precision cosmology*
- Zürcher, D., Fluri, J., Sgier, R., et al. 2022, *Monthly Notices of the Royal Astronomical Society*, 511, 2075

Appendix A: Log-normal simulations

The following plot demonstrates that log-normal simulations can mimic the non-Gaussian behavior of late-time fields. Indeed, the constraints obtained from the full-field approach (sampling the forward model) are much tighter compared to the standard power spectrum analysis.

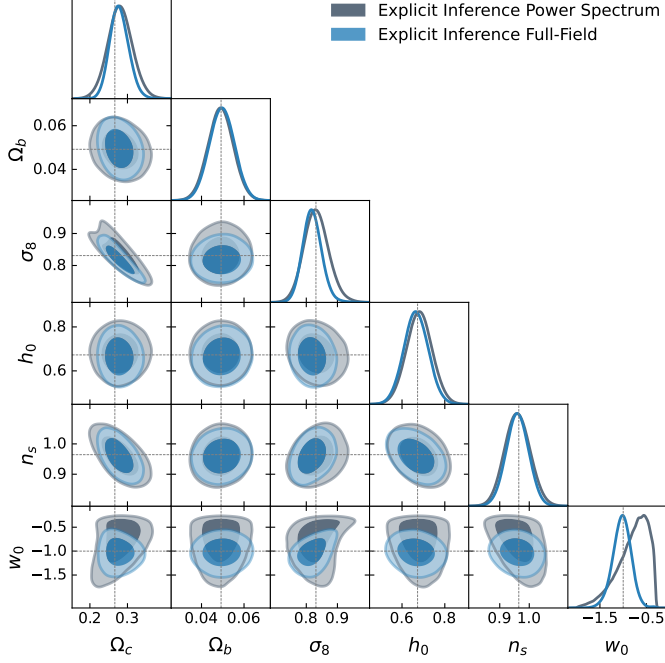


Fig. A.1. From log-normal simulated convergence maps at LSST Y10 quality we constrain the w CDM parameters using different inference techniques: power spectrum analysis (gray) and full-field analysis performed by sampling the forward model using an HMC sampler (blue).

Appendix B: Implicit inference benchmark

Appendix B.1: Methods

Appendix B.1.1: Learning the Likelihood Ratio

Neural Ratio Estimation (NRE) is based on the well-known likelihood ratio test. The idea is to test whether x has been generated by θ_0 or θ_1 through the following quantity:

$$r(x|\theta_0, \theta_1) = \frac{p(x|\theta_0)}{p(x|\theta_1)}. \quad (\text{B.1})$$

Using the *Likelihood Ratio Trick* this test can be cast as a binary classification problem where we train a classifier d_φ to learn the probability that x has been generated by θ_0 :

$$d_\varphi(x) = p(y = 1|x) = \frac{p(x|\theta_0)}{p(x|\theta_0) + p(x|\theta_1)}, \quad (\text{B.2})$$

$$r(x|\theta_0, \theta_1) = \frac{d_\varphi(x)}{1 - d_\varphi(x)}, \quad (\text{B.3})$$

with the two labels $y = 0$ and $y = 1$ corresponding respectively to $x \sim p(x|\theta_1)$ and $x \sim p(x|\theta_0)$.

Finally, this is generalized to all possible parameters θ by defining the label $y = 0$ as $(x, \theta) \sim p(x)p(\theta)$ and the label $y = 1$

corresponding to $(x, \theta) \sim p(x, \theta)$. This means that now the classifier learns

$$d_\varphi(x, \theta) = \frac{p(x, \theta)}{p(x)p(\theta) + p(x, \theta)} = \frac{p(\theta|x)}{p(\theta|x) + p(\theta)}, \quad (\text{B.4})$$

leading to the following likelihood ratio

$$r(x, \theta) = \frac{d_\varphi(x, \theta)}{1 - d_\varphi(x, \theta)} = \frac{p(\theta|x)}{p(\theta)}. \quad (\text{B.5})$$

Durkan et al. (2020) generalized this binary classification into a K multi-class classification and showed performance improvement when $K > 2$.

Similarly to NLE, given observed data x_0 , the approximated posterior is then obtained by sampling the distribution.

Appendix B.1.2: Learning the Posterior

Neural Posterior Estimation (NPE) aims to directly learn the posterior distribution. Similarly to NLE, NPE is based on neural density estimators such as NFs, whose goal is to learn $p_\varphi(\theta|x)$ from a set of parameters and corresponding simulations $(\theta, x)_{i=1..N}$. This can be done by using a conditional NF and minimizing D_{KL} :

$$\hat{\varphi} = \arg \min_{\varphi} \mathbb{E}_{p(x)} [D_{KL}(p(\theta|x) \| p_\varphi(\theta|x))], \quad (\text{B.6})$$

$$\implies \mathcal{L} = \mathbb{E}_{p(\theta, x)} [-\log p_\varphi(\theta|x)]. \quad (\text{B.7})$$

Note that, unlike NLE and NRE, for NPE no MCMC is needed to get samples from the posterior. This approach is very convenient if one has to evaluate the posterior distribution for different observations as it only requires a new evaluation of the learned model $p_\varphi(\theta|x)$.

Appendix B.2: Sequentially refined posterior

In most cases the prior $p(\theta)$ is significantly broader compared to the posterior $p(\theta|x = x_0)$, making it unnecessary to sample the entire parameter space. Instead, we would like to sample from a proposal $\tilde{p}(\theta)$ which denotes the most suitable regions. The question arises: How to choose this proposal $\tilde{p}(\theta)$ if we know neither the posterior location nor its size?

Starting from the prior, sequential methods offer a way to iteratively select this proposal by using the previous posterior approximation as the new relevant area and consequently refining the posterior at each iteration.

Each of the methods described above (NPE, NLE, and NRE) can be sequentially adjustable, however, there are some specificities to bear in mind: both SNLE (Papamakarios et al. 2018b) and SNRE (Durkan et al. 2020; Hermans et al. 2020) necessitate a sampling method or variational inference (Glöckler et al. 2022; Wiquist et al. 2021) at the end of each iteration to obtain the new parameters θ . SNPE (Papamakarios & Murray 2018; Lueckmann et al. 2017; Greenberg et al. 2019; Deistler et al. 2022) usually requires a costly correction of the approximated posterior since now minimizing the loss from Equation B.7 under the proposal $\tilde{p}(\theta)$ leads to

$$\tilde{p}(\theta|x) = p(\theta|x) \frac{\tilde{p}(\theta) p(x)}{p(\theta) \tilde{p}(x)}. \quad (\text{B.8})$$

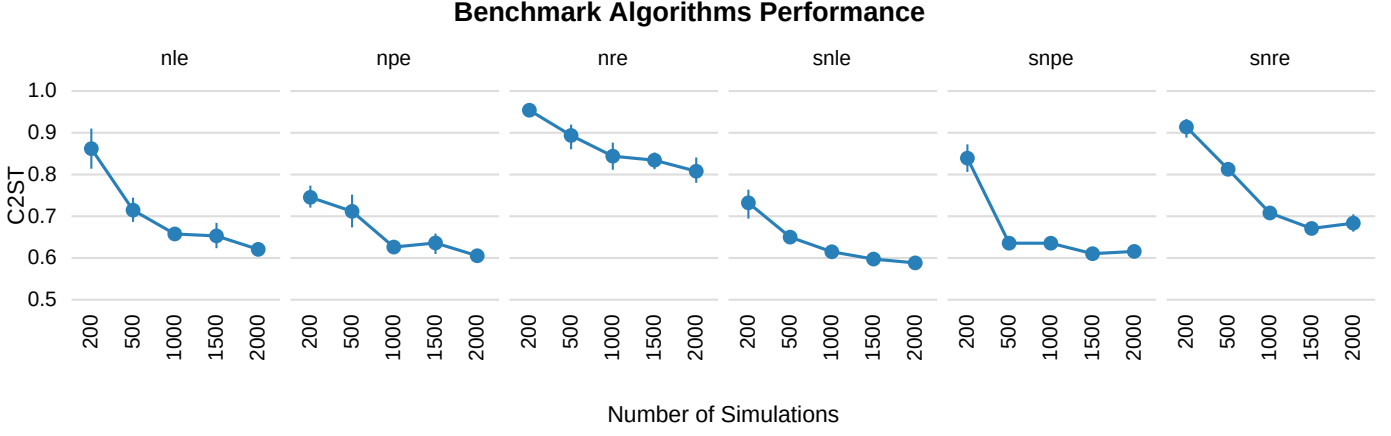


Fig. B.1. Implicit inference: quality of the cosmological posterior approximation as a function of the number of simulations used. We compare six methods using the default implementation of the `sbi` package: NLE, NPE, NRE, and their sequential counterparts SNLE, SNPE, and SNRE.

Appendix B.3: Results

To benchmark (S)NLE, (S)NPE, and (S)NRE methods, we use the same benchmark procedure as the one presented in Section 6. We use the `sbi` package for (S)NPE, (S)NLE, and (S)NRE methods. We choose to rely on `sbi`'s developers' expertise and use the default setting of `sbi` but optimizing the architectures would be interesting future work. For now, more detail about the implementation of these algorithms can be found in Appendix D subsection D.4.

Our numerical results in Figure B.1, suggest that NPE and NLE methods perform the best. The results also show that the sequential methods outperform their nonsequential analog. In particular, we find that SNPE and SNLE are the methods to favor as they allow to achieve a posterior quality of 0.6 with only 1 000 simulations.

Appendix C: MSE Minimization

In this section, we demonstrate that the following loss function

$$\mathcal{L} = \mathbb{E}_{p(x,z,\theta)} \left[\|g(x, \theta, z) - g_\varphi(x, \theta)\|_2^2 \right],$$

is minimized $\forall(x, \theta) \sim p(x, \theta)$ by

$$g_\varphi(x, \theta) = \mathbb{E}_{p(z|x,\theta)} [g(x, \theta, z)].$$

This proof is inspired by Remy (2023).

The optimal parameters of neural networks are typically chosen to cancel the following gradient

$$\begin{aligned} \frac{\partial \mathcal{L}}{\partial \varphi} &= \frac{\partial}{\partial \varphi} \mathbb{E}_{p(x,z,\theta)} \left[\|g(x, \theta, z) - g_\varphi(x, \theta)\|_2^2 \right] \\ &= \frac{\partial}{\partial g_\varphi} \mathbb{E}_{p(x,z,\theta)} \left[\|g(x, \theta, z) - g_\varphi(x, \theta)\|_2^2 \right] \times \frac{\partial g_\varphi}{\partial \varphi}. \end{aligned}$$

Since g_φ is by construction very unlikely to have null derivatives with respect to its parameters it means that

$$\frac{\partial}{\partial g_\varphi} \mathbb{E}_{p(x,z,\theta)} \left[\|g(x, \theta, z) - g_\varphi(x, \theta)\|_2^2 \right] = 0.$$

Thanks to Leibniz integral rule we can switch the gradient and integrals such that

$$\begin{aligned} \mathbb{E}_{p(x,z,\theta)} \left[\frac{\partial}{\partial g_\varphi} \|g(x, \theta, z) - g_\varphi(x, \theta)\|_2^2 \right] &= 0 \\ \mathbb{E}_{p(x,z,\theta)} \left[-2g(x, \theta, z) + 2g_\varphi(x, \theta) \right] &= 0 \\ \mathbb{E}_{p(x,\theta)} \left[-2\mathbb{E}_{p(z|x,\theta)} [g(x, \theta, z)] + 2g_\varphi(x, \theta) \right] &= 0. \end{aligned}$$

As $\mathbb{E}_{p(x,z,\theta)} [\|g(x, \theta, z) - g_\varphi(x, \theta)\|_2^2]$ is convex with respect to g_φ , it has a unique minimum that is reached when

$$g_\varphi(x, \theta) = \mathbb{E}_{p(z|x,\theta)} [g(x, \theta, z)].$$

Appendix D: Experiments Additional Informations

Codes for the compressor, the forward model, and the explicit full-field analysis are available at [sbi_lens](#). All codes relative to the benchmark of implicit inference techniques are available at [sbi_bm_lens](#).

Appendix D.1: Compressor Architecture

To compress the convergence maps of $5 \times 256 \times 256$ pixels into a 6 dimensional summary statistics we used a residual neural network (ResNet) (He et al. 2015) architecture. Specifically the ResNet-18. The ResNet-18 was trained under the VMIM loss function as described in subsection 6.3.

Appendix D.2: Neural Network Architecture to learn marginal gradients

To learn the marginal gradients $\nabla_\theta p(x|\theta)$ from the joint stochastic one $\nabla_\theta p(x, z|\theta)$ provided by the simulator, we used a neural network with 2 layers of 256 hidden units and Leaky ReLU activation functions. To test that we learned the correct marginal gradients we compared them against the gradients of a conditional NF trained with 10^5 simulations under the NLE loss.

Appendix D.3: NLE and ∂ NLE Architectures

For this study, the NF architecture remains fixed for the two methods, only the input changes: 1) we used only simulations;

2) we used simulations and the gradients of the simulator; 3) we used the simulations and the learned marginal gradients. Our conditional NF is a RealNVP (Dinh et al. 2017) of 4 coupling layers. Scale and shift parameters are learned using a neural network of 2 layers of 128 hidden units each. We used SiLU activation functions. To get the posterior from the learned likelihood, we used NUTS sampler. The epistemic uncertainty is approximated by training 7 NFs.

Appendix D.4: Standard Implicit Inference Architectures

To compare all the implicit inference techniques, we used the `sbi` package for (S)NPE, (S)NLE and (S)NRE methods.

For the sequential approach, the simulation budget was split across 5 rounds. To approximate the epistemic uncertainty we trained 5 NFs for each simulation budget.

(S)NLE - We used Papamakarios et al. (2018b) version of NLE and SNLE algorithm. In line with previous works (Durkan et al. 2020; Papamakarios et al. 2018b; Lueckmann et al. 2021; Greenberg et al. 2019), our neural density estimator is a Masked Autoregressive Flow (MAF) (Papamakarios et al. 2018a) with 5 autoregressive layers, each has two hidden layers of 50 units each. We used Tanh activation functions. Still in line with previous works, we used Slice Sampling schemes to recover the posterior distribution. Note that this is not the most efficient MCMC to explore high-dimensional or multi-modal spaces. However, since we are in a 6 almost Gaussian dimensional space this scheme works very well.

(S)NPE - We used NPE algorithm as formulated in Papamakarios & Murray (2018) but used as a neural density estimator a MAF instead of a Mixture Density Network (MDN). For SNPE algorithm we use Automatic Posterior Transformation (APT) by Greenberg et al. (2019). In line with previous works, our neural density estimator is a MAF with 5 autoregressive layers, each has two hidden layers of 50 units each. We used Tanh activation functions. For APT, to compute the atomic proposal, we used $M = 10$ atoms. The computational complexity of APT is $O(M^2)$ and as underlined by Lueckmann et al. (2021) more atoms are very demanding in terms of memory. In addition, unlike Greenberg et al. (2019) we found a difference in training time between $M = 10$ and $M = 100$ atoms.

Even though APT outperforms previous sequential NPE methods (Papamakarios & Murray 2018; Lueckmann et al. 2017), as reported by the APT paper itself Greenberg et al. (2019) and Durkan et al. (2020), this algorithm can suffer from leakage of posterior mass outside the prior support. To overcome this issue Deistler et al. (2022) introduced Truncated Sequential Neural Posterior Estimation (TSNPE).

(S)NRE - We used NRE algorithm as in Durkan et al. (2020) and used $K = 10$ class. In line with previous works (Durkan et al. 2020; Lueckmann et al. 2021), the K multi-class classifier is a residual neural network with two residual blocks of 50 hidden units and ReLU activation functions. Still in line with previous works, we used Slice Sampling schemes to recover the posterior distribution.

Appendix E: Additional convergence plots

We provide additional results showing the convergence of inference methods. Figure E.1 shows the contours evolution of the implicit inference posteriors approximated with NLE method. Figure E.2, Figure E.4, Figure E.3 and Figure E.5 show the evolution of the approximated mean and standard deviation of the posteriors approximated with NLE, ∂ NLE with joint gradients and marginal gradient, and the explicit inference methods. Figure E.6 shows the contours evolution of the explicit inference posterior. Finally, Figure E.7 displays the KDE approximation used to compute the C2ST metric of explicit inference method.

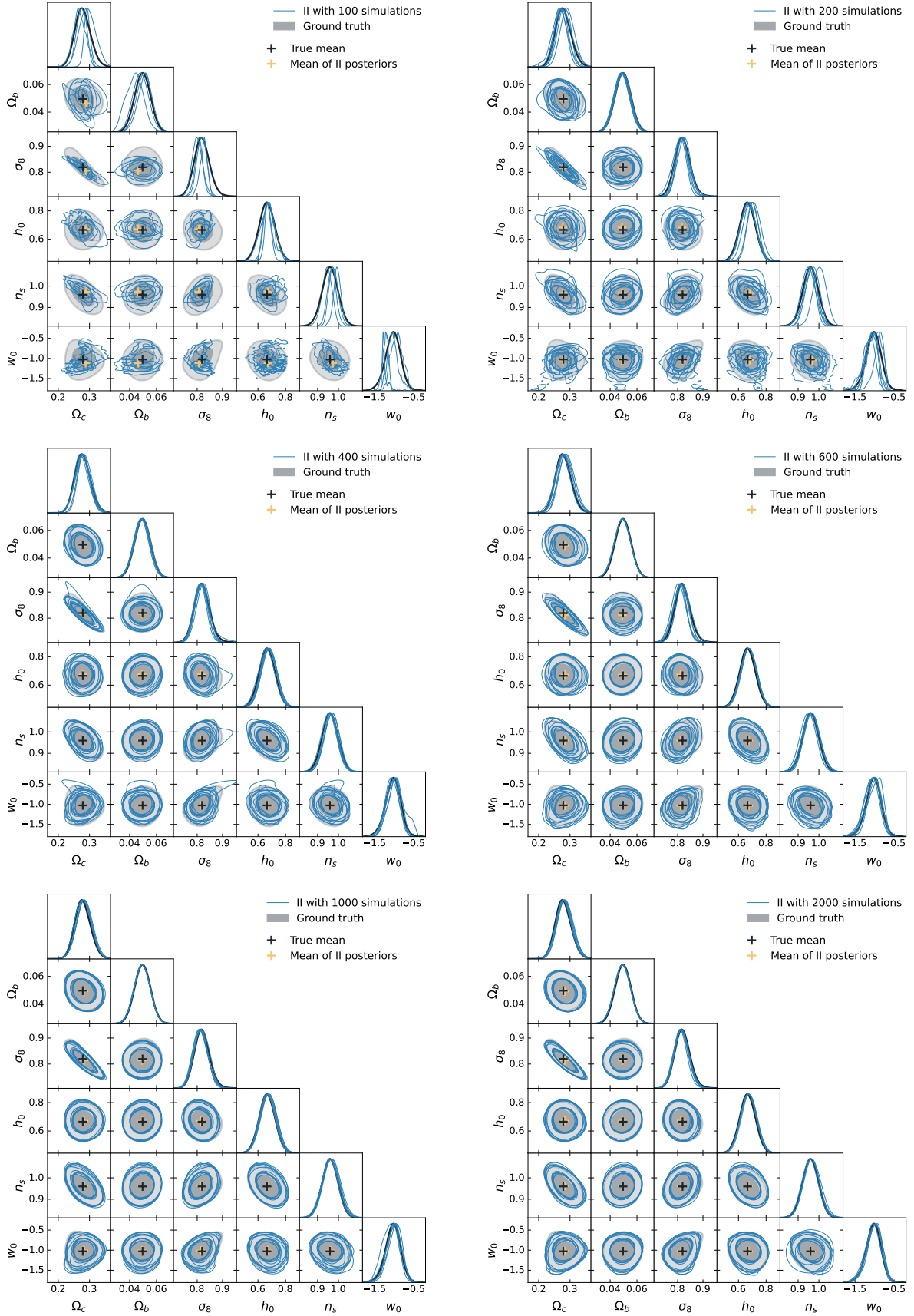


Fig. E.1. Evolution of implicit inference posteriors according to the number of simulations used to train the NF. The posteriors (blue contours) are approximated using the NLE method with simulations only. We train 5 NFs with the same architecture where only the initialization of the weights of the NF changes. Each blue contours correspond to the approximated posterior of one of these NFs. The ground truth (black contours) corresponds to the explicit inference posterior of 160 000 samples and the black marker corresponds to its mean. The yellow marker corresponds to the mean of the approximated posterior. With few simulations (e.g. 100 simulations) every NF predicts a different posterior and each prediction is overconfident. With a bit more simulations (e.g. 1 000 simulations), the posteriors are consistent and similar to the ground truth.

Implicit Inference (II) with simulations only

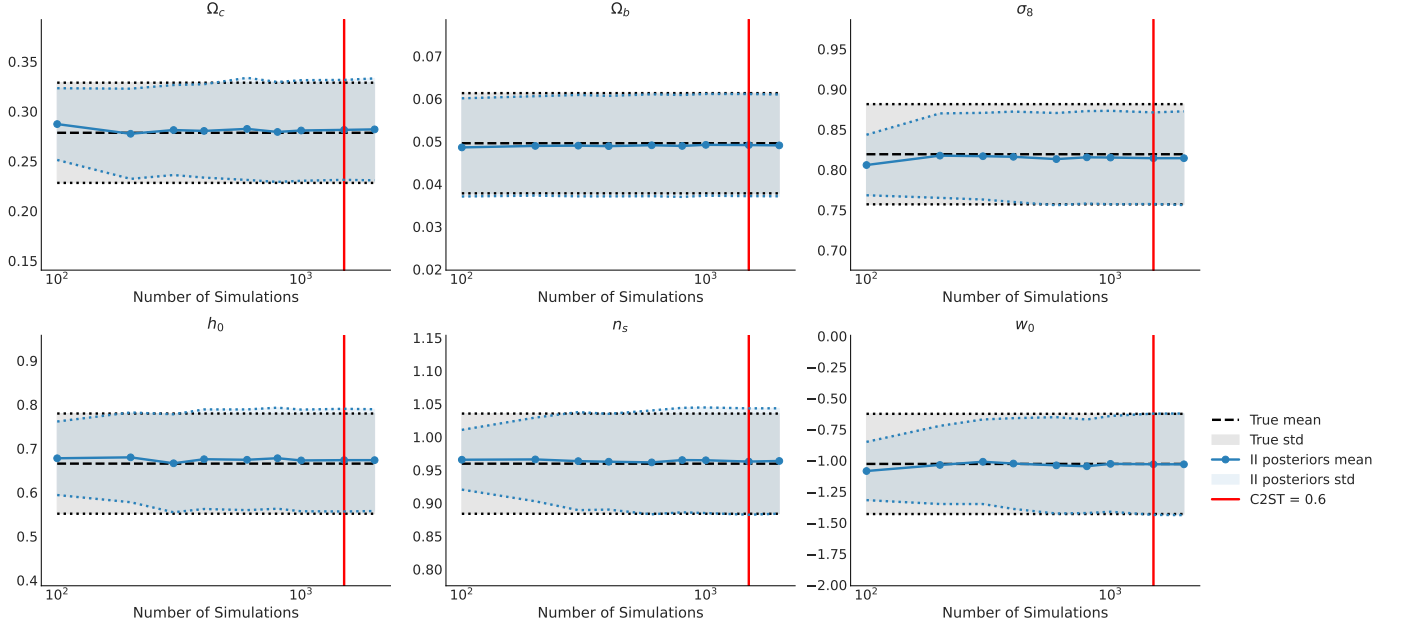


Fig. E.2. Evolution of the mean and standard deviation of the approximated implicit inference posterior as a number of simulations. The posterior is approximated using the NLE method with only simulations. We train five NFs with the same architecture where only the initialization of the weights of the NF changes. The blue line corresponds to the mean of the five approximated posteriors and the dotted line to the standard deviation. The dashed line corresponds to the mean of the ground truth (the explicit inference posterior of 160 000 samples), and the black dotted line to its standard deviation. The red line corresponds to the number of simulations for which the C2ST is equal to 0.6 (i.e. assume that the posterior is converged). Note that the C2ST can compare "higher moments" than the first and second moments of two distributions thus these plots can not serve as direct conclusions.

Implicit Inference (II) with simulations and gradients

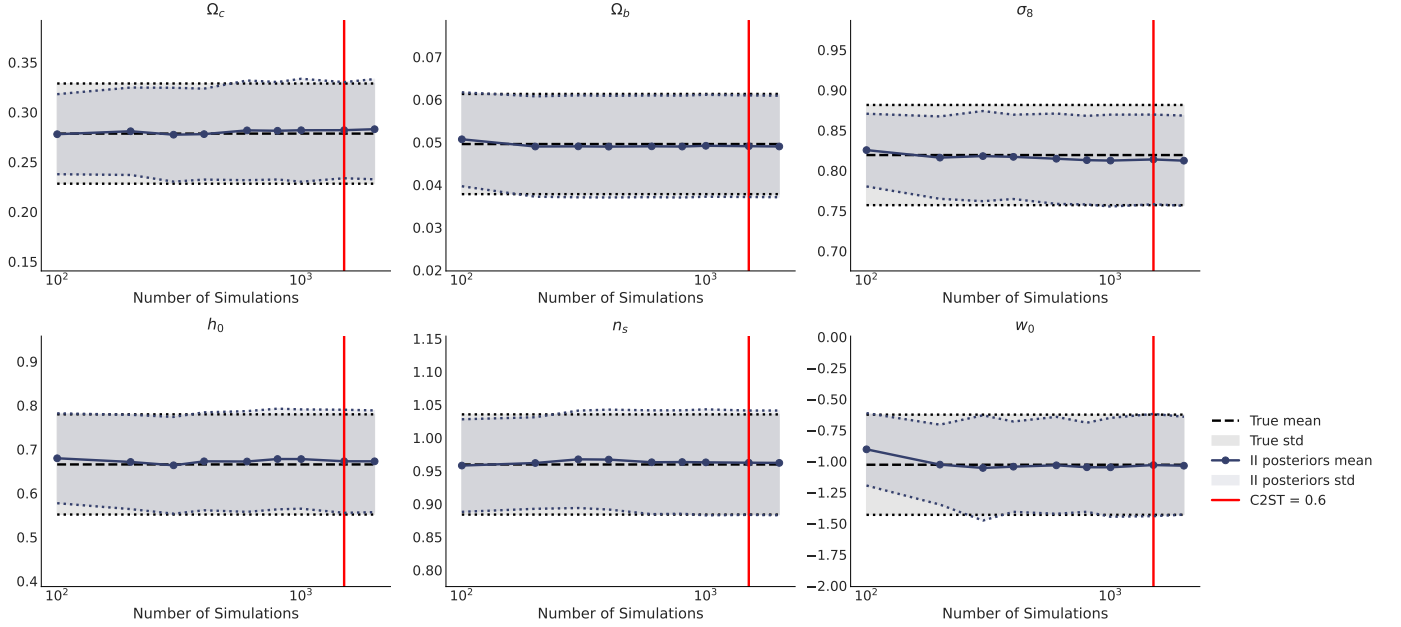


Fig. E.3. Same as the previous figure but this time the posterior is approximated using the ∂ NLE method with simulations and gradients.

Implicit Inference (II) with simulations and marginal gradients

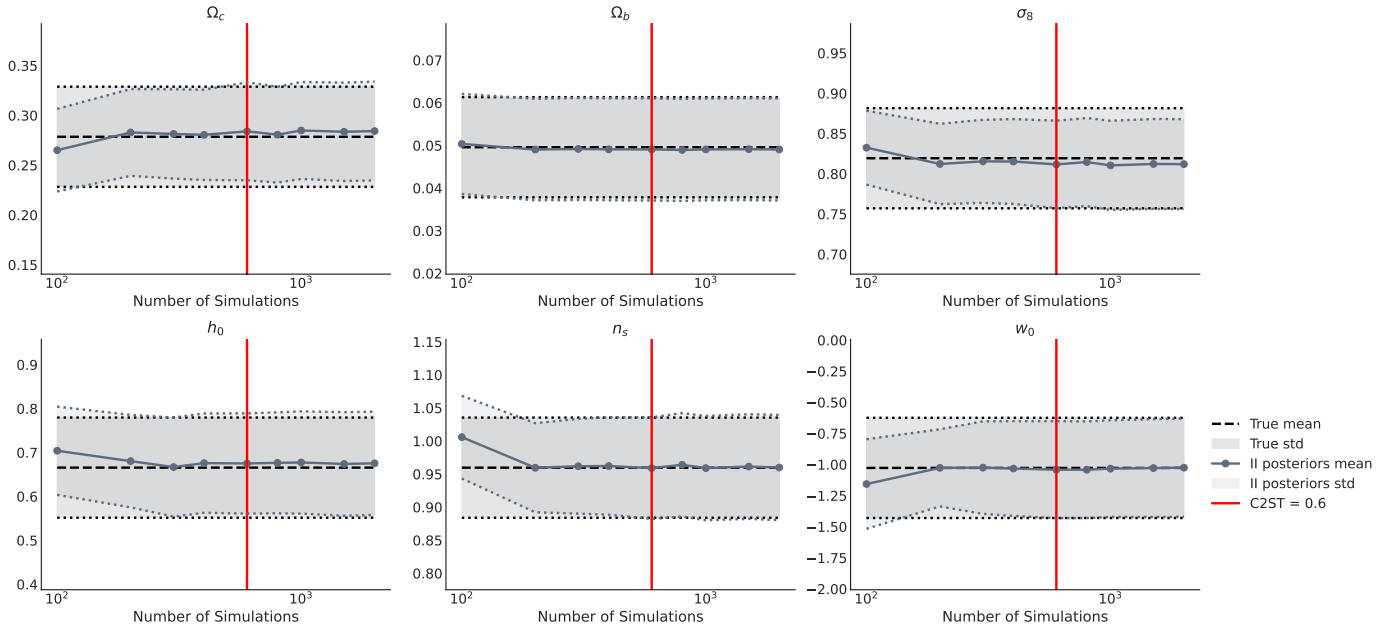


Fig. E.4. Same as the previous figure but this time the posterior is approximated using the ∂ NLE method with simulations and marginal gradients.

Explicit Inference (EI)

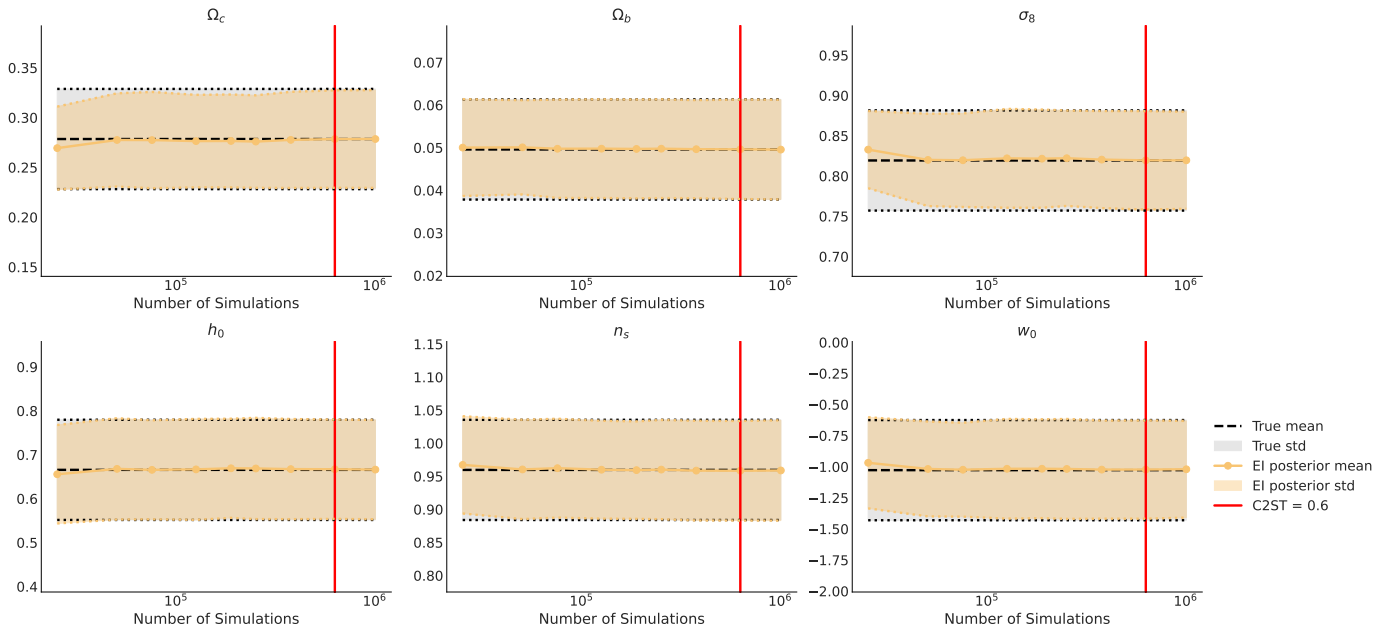


Fig. E.5. Evolution of the mean and standard deviation of the explicit inference posterior as a number of simulations. To get our 160 000 posterior samples (our ground truth) we use the NUTS algorithm. For each simulation budget N , we select the first N samples of this ground truth and compute its mean and standard deviation. The yellow line and dotted line correspond respectively to the mean and standard deviation. The black dashed line corresponds to the mean of the ground truth (of 160 000 posterior samples), and the black dotted line to its standard deviation. The red line corresponds to the number of simulations for which the C2ST is equal to 0.6 (i.e. assume that the posterior is converged). Note that the C2ST can compare "higher moments" than the first and second moments of two distributions thus these plots can not serve as direct conclusions.

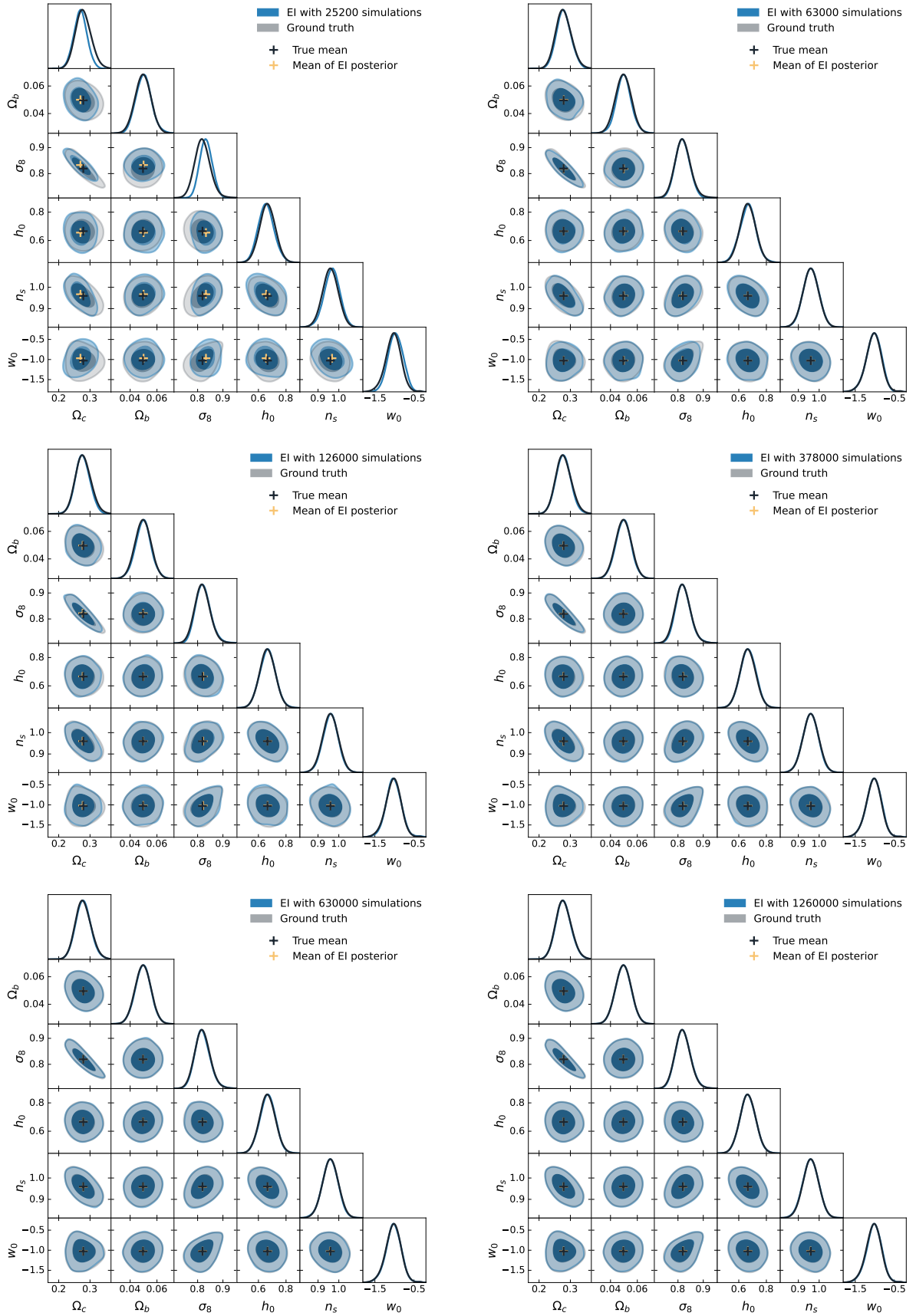


Fig. E.6. Evolution in terms of simulations of the explicit inference approximated posterior. The ground truth (black contours) corresponds to the explicit inference posterior of 160 000 samples. The blue contours denote the first N samples of the ground truth. Note that to get one sample our NUTS algorithm requires 126 simulations. The black marker corresponds to the mean of the ground truth. The yellow one, to the mean of the approximated posterior.

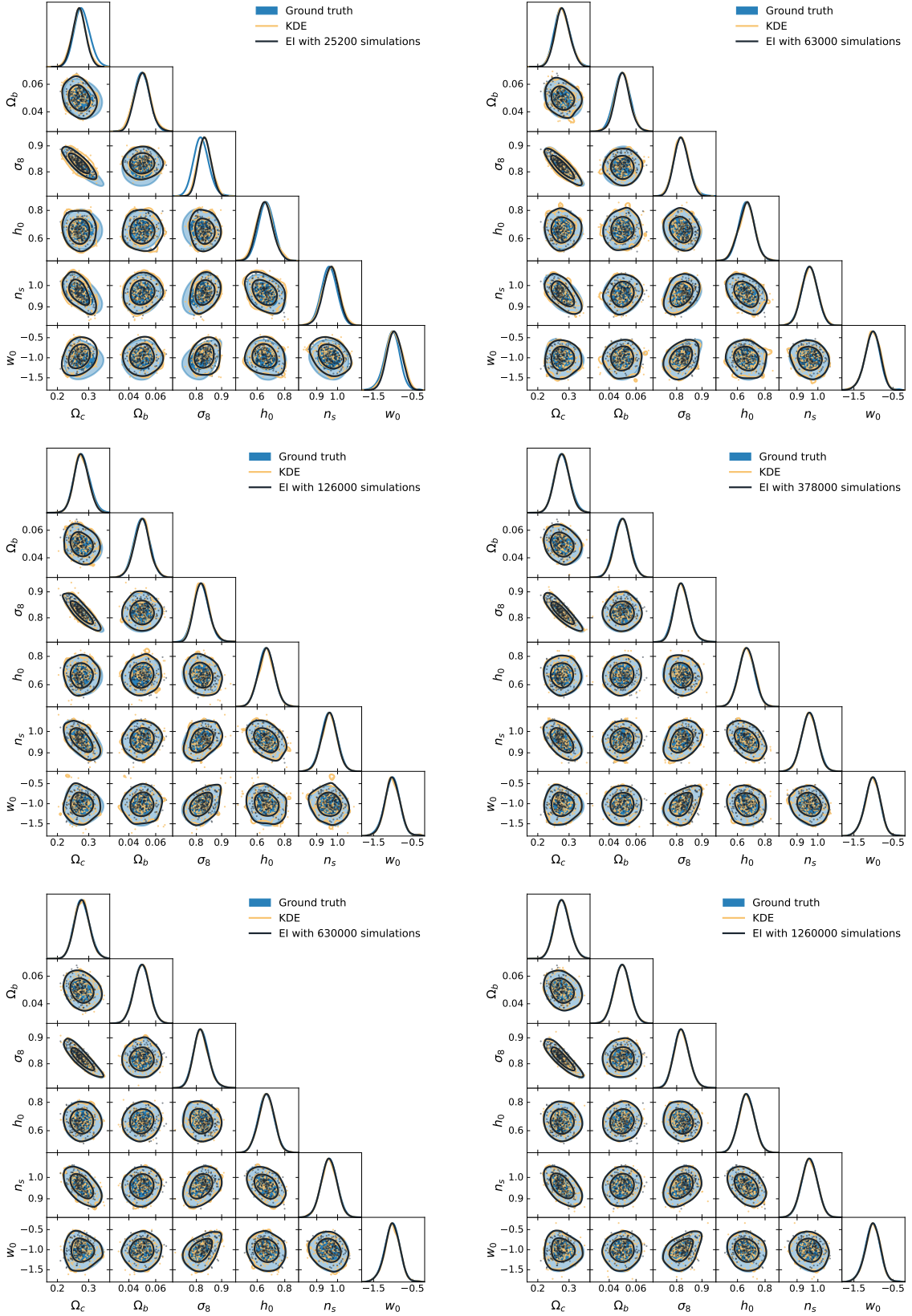


Fig. E.7. Samples of the KDE used to compute C2ST metric. In this paper we use the C2ST metric to evaluate the convergence of inference methods. This metric requires an equal number of simulations of the two distributions to be compared. To use the C2ST metric to benchmark the explicit inference method, inspired by the construction of contour plots that smooth the distribution (such as the one proposed by GetDist), we use a KDE to generate new samples. Specifically, we use a Gaussian kernel and set the bandwidth to match what GetDist would display for every number of explicit inference posterior samples (black contours). The yellow contours correspond to the contours obtained when fitting the N samples of explicit inference posterior and generating 20 000 samples from the KDE. We use a very small smoothing scaling value to display the posterior contours of the KDE with GetDist. The blue contours denote the ground truth of 160 000 samples.